

Article

Predicting the Porosity in Selective Laser Melting Parts Using Hybrid Regression Convolutional Neural Network

Nawaf Mohammad H. Alamri *, Michael Packianather and Samuel Bigot 

School of Engineering, Cardiff University, Queen's Buildings, 14-17 The Parade, Cardiff CF24 3AA, UK

* Correspondence: alamrinm@cardiff.ac.uk

Abstract: Assessing the porosity in Selective Laser Melting (SLM) parts is a challenging issue, and the drawback of using the existing gray value analysis method to assess the porosity is the difficulty and subjectivity in selecting a uniform grayscale threshold to convert a single slice to binary image to highlight the porosity. This paper proposes a new approach based on the use of a Regression Convolutional Neural Network (RCNN) algorithm to predict the percent of porosity in CT scans of finished SLM parts, without the need for subjective difficult thresholding determination to convert a single slice to a binary image. In order to test the algorithm, as the training of the RCNN would require a large amount of experimental data, this paper proposed a new efficient approach of creating artificial porosity images mimicking the real CT scan slices of the finished SLM part with a similarity index of 0.9976. Applying RCNN improved porosity prediction accuracy from 68.60% for image binarization method to 75.50% using the RCNN. The algorithm was then further developed by optimizing its parameters using Bees Algorithm (BA), which is known to mimic the behavior of honeybees, and the hybrid Bees Regression Convolutional Neural Network (BA-RCNN) produced better prediction accuracy with a value of 85.33%.

Keywords: deep learning; regression convolutional neural network; bees algorithm; selective laser melting; artificial porosity images



Citation: Alamri, N.M.H.; Packianather, M.; Bigot, S. Predicting the Porosity in Selective Laser Melting Parts Using Hybrid Regression Convolutional Neural Network. *Appl. Sci.* **2022**, *12*, 12571. <https://doi.org/10.3390/app122412571>

Academic Editor: Christian Spielmann

Received: 23 October 2022

Accepted: 5 December 2022

Published: 8 December 2022

Publisher's Note: MDPI stays neutral with regard to jurisdictional claims in published maps and institutional affiliations.



Copyright: © 2022 by the authors. Licensee MDPI, Basel, Switzerland. This article is an open access article distributed under the terms and conditions of the Creative Commons Attribution (CC BY) license (<https://creativecommons.org/licenses/by/4.0/>).

1. Introduction

Additive manufacturing (AM) is defined in ISO/ASTM 52900:2021 standard [1] as a process that builds parts by joining a material layer by layer, using 3D model data. The standard defined seven process categories for AM, namely binder jetting, directed energy deposition, material extrusion, material jetting, powder bed fusion, sheet lamination, and vat photopolymerization. AM are also referred to as rapid prototyping, 3D printing, layered manufacturing, and digital manufacturing [2]. There are two levels for AM processes. The first one is the digital level where the CAD model is prepared, converted to stl.file, and where machine control strategy is generated (e.g., CAM, G code). The second level is the physical level which contains part manufacturing using one of the seven processes mentioned previously [3]. Initially, AM or 3D printing technologies were used mainly for rapid prototyping, but with improvements in the reliability and efficiency of AM processes, as well as in the material properties of the components produced, they are increasingly used in creating complicated customized parts, visualizing tools in design, and producing serial components with small volume. In the future, it might be used for manufacturing clothes, creating food confections, and human organs [2].

There are many advantages for using AM processes, such as the flexibility in the producible designs, the facilitated customization of products, and the capability to print highly complex structures. However, many challenges and drawbacks remain. More specifically, some disadvantages are the stair-stepping effect that appeared in the manufactured product, void formation between the layers resulting from binding reduction, and mechanical proprieties and microstructure variation [4].

The applications for using AM include prototyping during the product development phase, producing products in pilot series production where injection molding costs are high, and creating complex geometry parts which cannot be produced by other means of manufacturing [5]. This gives the edge to AM among manufacturing processes. For example, it allows the integration of additional functionality in components, such as the production of repeated patterns internally. Thus, AM has the capability for combining internal complex structures with more regular outer geometries, reducing weight while keeping structural and aesthetic integrity, as can be done in the manufacturing of a bike frame. Furthermore, applications are emerging in the context of the highly regulated aerospace and automotive sector. For instance, metal parts suitable for aircraft were directly manufactured using titanium material [4], reducing lead time by 30–70%, non-recurring fabrication costs by 45%, and reducing the manufacturing cost for producing low-volume parts by 30–35%. However, metal-based AM such as Powder Bed Fusion (PBF) still has many issues such as porosity, part deformation, and cracks formations [6] that remain to be tackled. Among them, the presence of porosity is particularly critical, as this can have significant effects on the mechanical properties of components, cause failures for the structure, and may decrease the strength and modulus of Young [7]. Thus, the focus of this paper is to facilitate the study of porosity formation in AM.

A common approach in the study and optimization of emerging manufacturing techniques is the use of Artificial Intelligence (AI) technologies. AI facilitate intelligent systems development [8] to maximize the efficiency and productivity of manufacturing machines. AI techniques include Artificial Neural Network (ANN), inspired by the biological human brain. It can be used to investigate the complex relationships in big data [9] and extract meaningful implicit patterns to predict complex systems' future states [10].

Deep Learning (DL) techniques are established as an extension to the capabilities of ANN, as they extract features, automatically producing better learning capability [11]. Convolutional Neural Network (CNN) is one of the most used DL techniques which deals mainly with image data [9], and it can be integrated with other intelligent swarm optimization algorithms to optimize its parameters to improve CNN performance in analyzing a large number of images for classification and prediction problems [12]. Thus, CNN is an effective DL network that can be applied in the manufacturing context and therefore, in this paper context, to analyze porosity images related to AM facilitating the optimization of the process.

This study aims at facilitating the accurate prediction of porosity percentage occurring in PBF when analyzing CT scans of parts. This is achieved using a new Regression Convolutional Neural Network (RCNN) algorithm. As the training of such RCNN would require a large amount of costly experimental data to generate real CT scans, it was decided to first train, test, and validate the new algorithm using artificial porosity images mimicking real CT scan slices. Following this, the RCNN was further optimized using the Bees Algorithm (BA), which mimics the behavior of honeybees to produce better prediction accuracy, as was demonstrated by the authors in a previous paper that described the hybrid Bees Regression Convolutional Neural Network (BA-RCNN) [12].

The paper structure is as follows: Section 2 summarizes the main AM processes and provides a review of PBF, highlighting the gaps that remain to be addressed to improve the process performance. Section 3 describes a new method developed to create artificial porosity images that mimic real CT scan slices of finished SLM parts, and Section 4 presents the predicted percent of porosity using RCNN and proposes a novel hybrid BA-RCNN algorithm in order to improve the prediction accuracy. Finally, Section 5 concludes the study and suggests the future directions.

2. Powder Bed Fusion

This section presents a review of the PBF process, showing the way of working, thermodynamical phenomena, parameters, open issues, and state-of-the-art studies.

2.1. PBF Definition and Way of Working

As shown in Table 1, Reference [2] presented many AM processes that can be used for the production of complex parts, and PBF is one of the most promising due to its ability to process a wide range of hard metals.

Table 1. Additive layer manufacturing processes (Farinia Group).

No.	Process	Techniques	Materials
1	Powder bed fusion	Direct metal laser sintering (DMLS), selective laser sintering (SLS), selective laser melting (SLM) and electron beam melting (EBM)	Polymers, metals: miraging steel, stainless steel 316L, 15-5PH, nickel-based superalloys: Hastelloy X, Inconel 625, Inconel 718, chrome-cobalt, titanium TA6V, aluminum AISi10mg
2	Material extrusion	Fused deposition modelling (FDM)	Thermoplastic filament
3	Material Jetting	PolyJet (PJ)	Photopolymers and wax-like materials
4	Binder jetting	Binder jetting	Photopolymers and wax-like materials
5	Sheet lamination	Laminated object manufacturing (LOM), paper lamination technology (PLT), ultrasonic additive manufacturing (UAM)	Adhesive-coated papers, metal tapes and foils, plastic sheet material
6	Vat photopolymerization	Stereolithography (SLA), digital light processing (DLP)	Light curable resin
7	Directed energy deposition	Laser engineered lens shaping (LENS), direct metal deposition (DMD), laser metal deposition (LMD), blown powder, laser cladding	Metals such as aluminum nickel-based alloys

Reference [3] presented AM manufacturing technologies classification based on materials according to ISO/ASTM 52900, as shown below in Figure 1:

PBF processes are metal-based AM where the laser beam scans at a controlled speed selected locations of a powder bed and then fuses the powder to obtain solid material [13] layer by layer by either partial melting, such as in SLS, or full melting, such as in the metal-based process SLM [6]. Reference [13] presents Figure 2, which illustrates the elements of laser-based PBF process.

The first crucial part of the SLM process is the build job preparation for any given 3D model. It consists of four main steps: geometry importation, alignment/orientation within a build envelope (critical as surfaces with an angle less than 45° need to be supported), support creation to allow stable processing conditions, and finally slicing based on machine-specific requirements. After preparing and loading a build job onto a machine, the manufacturing process can be initiated starting with the alignment of the recoating device or levelling of the substrate to enable the deposition of powder. Next, the laser scans a specific area based on a predefined scanning strategy and controllable parameters to selectively solidify the material. After finishing a layer scanning, the build plate is moved down, and new powder is deposited on top of the build area to produce a new layer [14]. Reference [14] presented Figure 3 that illustrates the influential factors of a typical SLM process:

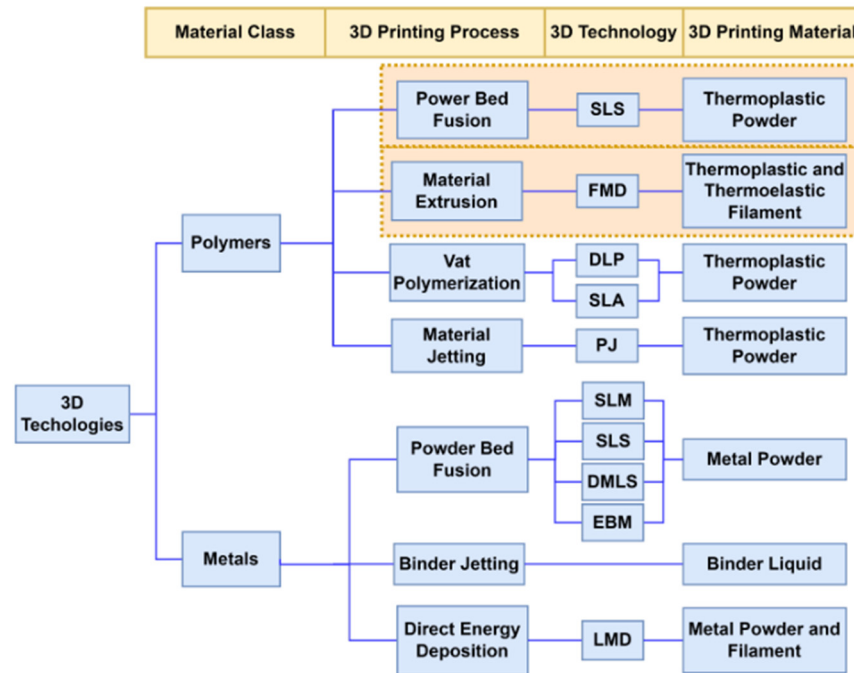


Figure 1. AM technologies classification according to ISO/ASTM 52900 [3].

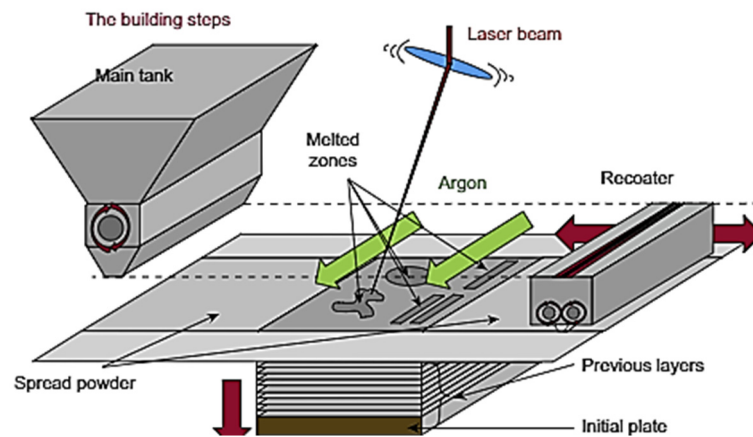


Figure 2. Elements of powder bed fusion process [13].

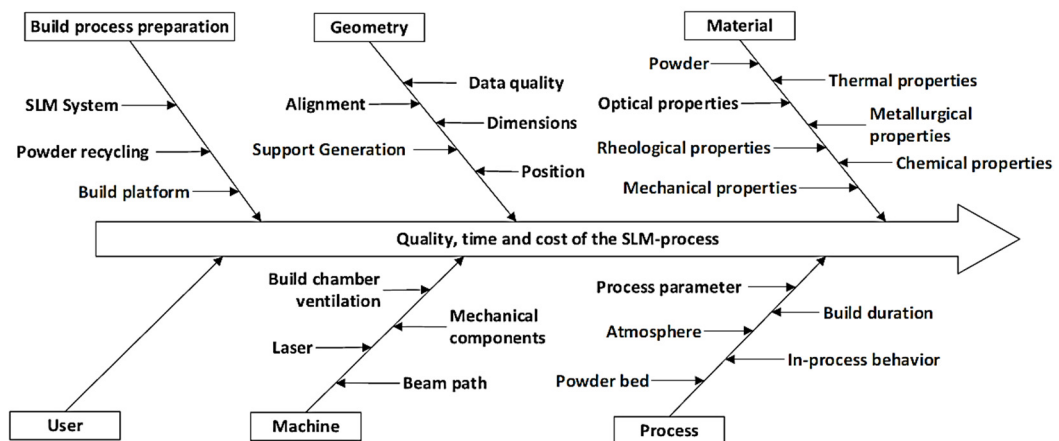


Figure 3. Ishikawa diagram of influential factors in SLM process [14].

There are many applications of the SLM process in real life, such as in the medical field with dental implants (highly complex, small in dimension, and one-off patient products) or with specialized surgery equipment. Another large field is in the aerospace industry where it is hard to manufacture materials, such as nickel-based superalloy, and requires high quality, complex shapes, and low to medium production lots like hydraulic manifolds [14].

2.2. Thermodynamical Phenomena

The PBF process involves complicated thermodynamical phenomena and physio-chemical behavior, as powder particles are melted using a laser beam with high energy. Thermodynamic monitoring is important to control the performance of the process, but it is difficult as the molten pool is small and moves quickly. Recently, numerical modelling has been developed to study the physical mechanism deeply. Metal SLM involves principles for multiscale coordinate control, and they include deformation and stress (macroscale), melting behavior and laser absorption (mesoscale), and the development of microstructure (microscale) [15].

The limited energy on the powder bed and low operating temperature resulting from low laser power value in SLM lead to generating residual pores between the neighboring small molten pools. The low temperature decreased the liquid surface tension, leading to the melt flow [15]. These conditions cause a remarkable reduction of the melt pool convection, and simultaneously lead to a weakening of the melt migration between the current and solidified neighboring tracks. As a result, the porosity is shown obviously on the top surface and cross-section of the SLM part. Conversely, increasing the laser power results in a larger molten pool size with a longer lifetime of the liquid. The considerable laser energy input leads to an intensified convection within the melt pool with sufficient melt migrations between the high laser power tracks, which produce high-quality SLM parts without distinct defects on both the cross-section and top surface. In addition, cellular morphology is presented with the microstructure surrounding the tracks with no obvious defects. Reference [15] presented the following Figures 4 and 5 for the top surface morphology of the produced Inconel 718 part with two different laser powers, 90 W and 120 W.

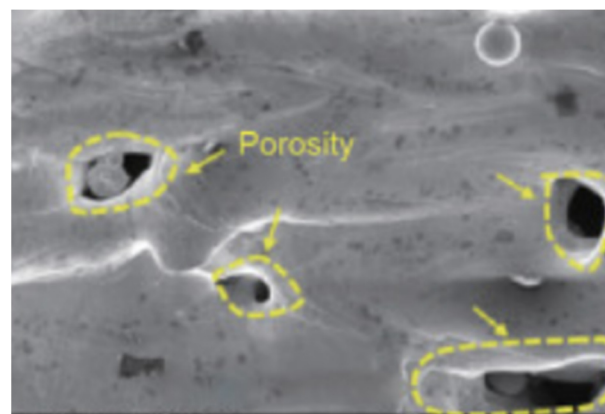


Figure 4. Top surface morphology with laser power of 90 W [15].

Therefore, with a low laser power value of 90 W, irregularly shaped porosity was shown distinctively in the tracks where heat transfer and limited mass occurred. Increasing the laser power value to 120 W decreased the porosity. Therefore, producing high-quality Inconel 718 parts are achievable with optimal laser power that can be specified using mesoscale simulation and analysis [15].

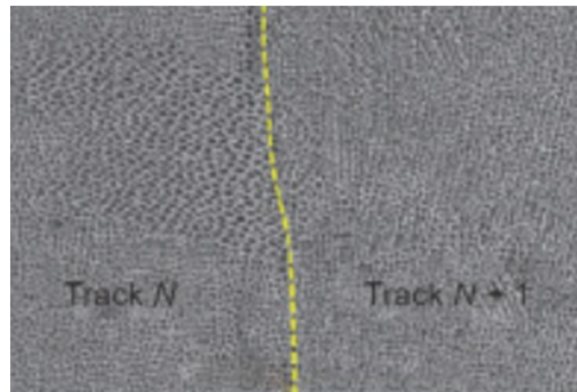


Figure 5. High magnification microstructure morphology of top surface with laser power of 120 W [15].

2.3. Parameters

The process parameters for PBF can be classified into four categories. The first one is the parameters related to the laser which include laser power, spot size, wavelength, pulse frequency, and duration. The second category is scanning strategy parameters (scanning speed, scanning patterns, scanning spacing, and layer thickness). The third category is the set of powder-related parameters which include powder bed density, particle shape, distribution and size, material properties, and layer thickness. The last category is the parameters related to temperature, including the temperature of the powder bed and feeder and temperature uniformity [13].

2.4. Open Issues

Metal-based AM has many gaps that need to be addressed, such as porosity, cracks, and part deformation [6], but as mentioned previously, porosity is a challenging issue due to its effect on the mechanical properties, structural integrity, strength, and Young's modulus of the produced material. There are three main pore types, namely gas, keyholes, and lack of fusion pore [7]. The following subsection will explain each type, showing its characteristics and mechanism of formation.

2.4.1. Gas Porosity

Gas pores belong to the most common type of pores. They are the most spherical and the smallest type. It is characterized by smooth edges and a wide range of sizes from submicron to several microns [16]. The following Figure 6 shows an illustrative example of the gas porosity using the scanning electron microscope (SEM) [16]:

Gas pores are connected to trapped gas that might have different sources of origin, either during or before the process starts, such as the entrapped gas in the powder of the alloy during the process of gas atomization. However, increasing the laser power or decreasing the scanning speed might enlarge this type of pore. Reference [16] fabricated SLM samples at a specific scanning speed of 1200 mm/s and with laser power values between 225 W to 375 W to investigate the gas porosity evolution. They found that increasing the laser power from 225 W to 300 W leads to raising the fraction of gas pore from 1.3% to 1.6% but increasing the laser power further from 300 W to 375 W reduced the fraction to 0.7% as the thermal gradient between the center and boundary of melt pool is increased, which leads to facilitating the process of outgassing. Therefore, it was concluded that it is difficult to fully understand the effect of SLM process parameters on gas porosity formation, since it is a dynamic process that involves pore nucleation, growth, and outgassing during rapid solidification [16].

2.4.2. Keyhole Porosity

Keyhole pores arise from energy input excess with an energy density value of more than 110 J/mm³ [16], which is a result of increasing the laser power or decreasing scanning

speed. It is characterized by large-size cavities reaching hundreds of microns and tended to be near-spherical in shape, so sometimes it is difficult to distinguish between large gas pores and keyhole pores. The following Figures 7 and 8 show the 3D view of the keyhole pore at a laser power value of 195 W and scanning speed value of 400 mm/s and different shapes of 2D images [6].

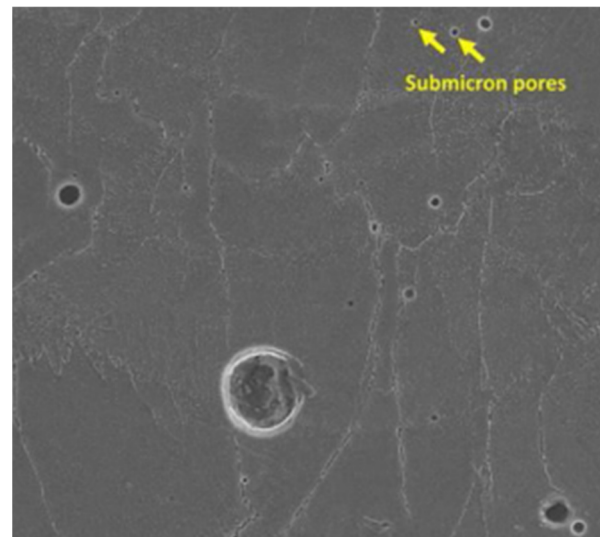


Figure 6. Illustrative example of gas porosity using SEM [16].

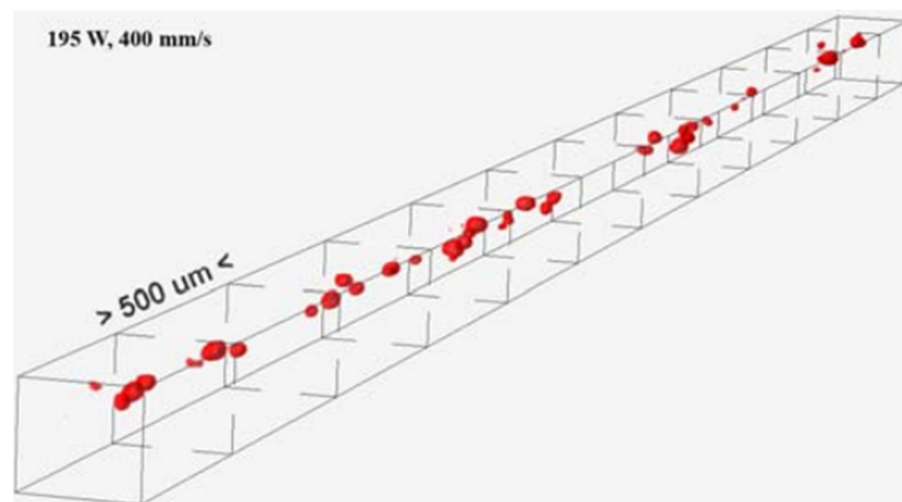


Figure 7. 3D view of keyhole pores [6].

Unlike gas pores, the surface and contour are bumpy, and these cavities are the most common type of keyhole porosity that appear in the SLM part [16]. It is caused when trapping bubbles of vapor within the melt pool [6], changing the melting mode from conduction to keyhole mode at high laser energy intensity leads to the formation of this type of pore. In the conduction mode, the laser energy input is low to moderate which mediates the heat transfer through conduction. The material melting happens in this mode without vaporization which results in less porosity, but in the keyhole mode, the high laser intensity causes metal evaporation which generates recoil pressure at the bottom of the melt pool. The instability of the dynamic behavior in the melt pool leads to the formation of keyhole porosity with near-spherical morphology at the bottom of the melt pool, which acts as a stress concentrator, causing material property deterioration [16].

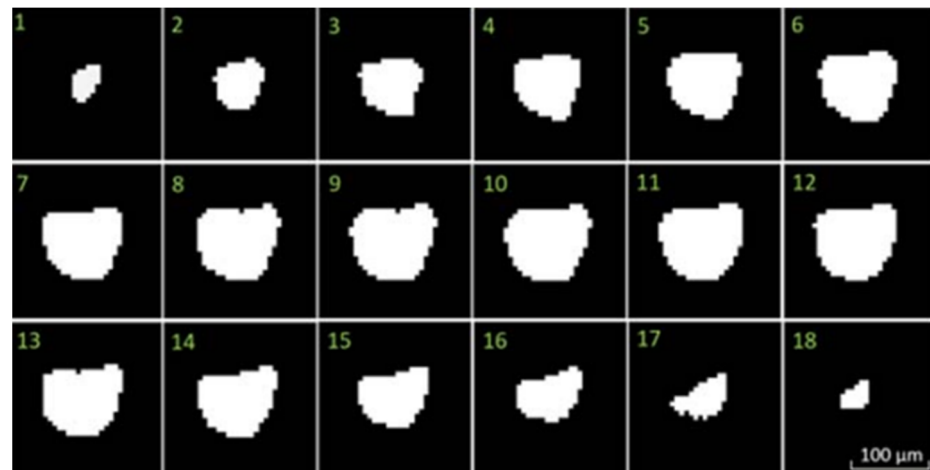


Figure 8. 2D images of different keyhole pores morphologies [6].

2.4.3. Lack of Fusion Porosity

Lack of fusion pores have irregular voids morphology that commonly appeared in SLM alloy. They are featured with large sizes, reaching hundreds of micrometers as shown in the following Figure 9 [16]:

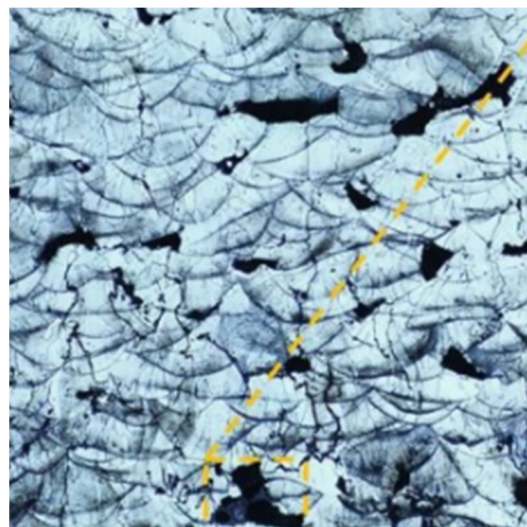


Figure 9. Lack of fusion pores morphology [16].

Irregular voids are formed because of un-melting in some regions caused by the reduction in energy density, which is generally a result of the low value of laser power or fast scanning speed [16]. The energy density is a function consisting of laser power, scanning speed, layer thickness, and hatch distance, and these parameters have a significant effect on pores formation [6]. Having insufficient laser energy to induce the overlapping between the adjacent layers leads to the formation of this type of pore. Additionally, the high reflectivity and dense oxide presence on the powder particles' surface might form such defects as the laser penetrability is lowered [16].

Thus, when optimizing the SLM process, it is essential to accurately study the pore formation occurring when using various combinations of parameters.

2.5. State of the Art Studies

Detecting porosities in PBF processes has a significant contribution to improving part quality [17]. The porosity during the laser additive manufacturing process was monitored

using a deep learning-based method, namely convolutional neural network, that predicts the porosity based on melt pool cross-section images acquired by coaxial camera [18]. The model achieved an accuracy of 91.2% in detecting porosity occurrence, and all misclassified samples have pores less than 50 μm . This limitation in detecting micropores is one of the issues in applying convolutional neural network for pores prediction. Similarly, a lack of fusion porosity was predicted based on melt pool data collected during the selective laser melting process, and the DMP monitoring system was used to monitor the melt pool during the processing with titanium alloy material. Next, they created an algorithm that correlated the porosity with melt pool monitoring data, which achieved 90% prediction sensitivity for events with a lack of fusion pores greater than 160 μm volume [19].

Recently, acoustic signals have been used in porosity classification, particularly in achieving the balance between classification accuracy and spatial resolution in porosity detection. High sensitivity fiber Bragg grating sensor was adopted to collect acoustic signals for airborne. The time span for each running window was 160ms, and 300 patterns represented each of the three porosity levels without overlapping between training and testing set in terms of the running window. The parts with different porosity levels were classified using spectral CNN with a classification accuracy between 83–89% [20].

Using CT scans of sample parts, there is a problem related to assessing accurately the porosity in SLM parts [21]. One main drawback is clear when using gray value analysis to assess the porosity of SLM parts visible in CT scan slices. The difficulty is the subjectivity in selecting an appropriate grayscale threshold that would convert a single slice into binary images highlighting defective regions, as well as determining the true level of porosity. For example, in Figure 10 when an inappropriately low grayscale threshold is used for binary image conversion for the original slice, an amount of tiny undesired white spots is not filtered, as shown in Figure 10b. However, adopting a high threshold causes significant alterations in the morphological features of the defective area, more specifically near the boundary, as shown in Figure 10c. These thresholds would result in significantly different predictions of porosity levels.

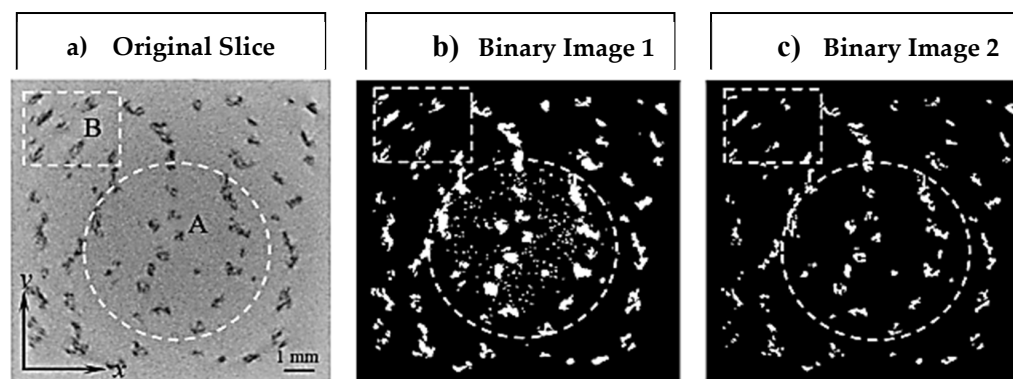


Figure 10. Original slice and binary images [21].

To evaluate this issue further, the authors of this study [21] proposed an empirical method to estimate the porosity in finished SLM parts using a naturalized threshold for CT scan slices. When compared with the Archimedes method, they found similar increasing or decreasing trends in the predicted percentage of porosity, and concluded that the naturalized grayscale threshold is not the best method for porosity estimation in CT scan slices due to radiodensity variation and CT setup mutual influence. Thus, compensating for these variations is difficult with a unique grayscale [21]. This limitation is found in one of the main existing methods used in porosity estimation, along with the Archimedes method, as mentioned in [22]. Thus, this paper addresses this gap by proposing a new approach based on the use of a Regression Convolutional Neural Network (RCNN) algorithm to predict the percent of porosity in CT scans of finished SLM parts, without the need for subjective difficult thresholding determination to convert single slice to a binary image. In

order to test the algorithm, as the training of the RCNN would require a large amount of experimental data, artificial porosity images mimicking real CT scan slices of the finished SLM part will be created using a new efficient method explained in detail in the following section.

3. Artificial Porosity Images Creation for SLM Parts

Training CNN algorithms would require a large amount of experimental data, which is expensive for SLM parts [23], since there are many types of production costs for pre-processing, processing, and post-processing costs, including preparing geometry data, CAD model, machine setup, material cost, building up the part, and postprocessing cost [24], so producing a large amount of porosity images to train RCNN is not cost-effective. This section proposes a new efficient approach of creating artificial keyhole porosity images mimicking the real CT scan slices of finished SLM parts that can be used in the research environment effectively and efficiently, in particular to validate the training of an accurate RCNN for the automatic prediction of porosity in CT scans of SLM parts. The steps of creating the artificial porosity images are illustrated in Figure 11, followed by subsections explaining the steps in detail.

3.1. Establishing Regression Equations

The formulation of two regression equations is based on the laser power and the scanning speed data found in [6]. The first equation correlates the number of pores (Y) with the laser power (X1) and the scanning speed (X2), and the second equation correlates the pores' diameters (Y) with the same parameters (X1 and X2). The data used to establish the two equations are related to keyhole porosity and they will be used as a demonstration for an example of pore types' formation.

Table 2 shows the corresponding number of pores for each combination of laser power and scanning speed.

Table 2. Number of pores for each laser power and scanning speed combination [6].

No.	Laser Power (W)	Scanning Speed (mm/s)	Number of Pores in 2.6 mm ³ Volume
1	195	200	101
2	175	200	121
3	150	200	121
4	125	200	101
5	195	400	41
6	175	400	75
7	150	400	55
8	195	600	4
9	125	400	30
10	175	600	19
11	150	600	4
12	195	800	0
13	175	800	1
14	125	600	2
15	150	800	0
16	195	1000	0
17	175	1000	0
18	125	800	0
19	195	1200	0
20	150	1000	1
21	175	1200	0
22	125	1000	0
23	150	1200	0
24	125	1200	0

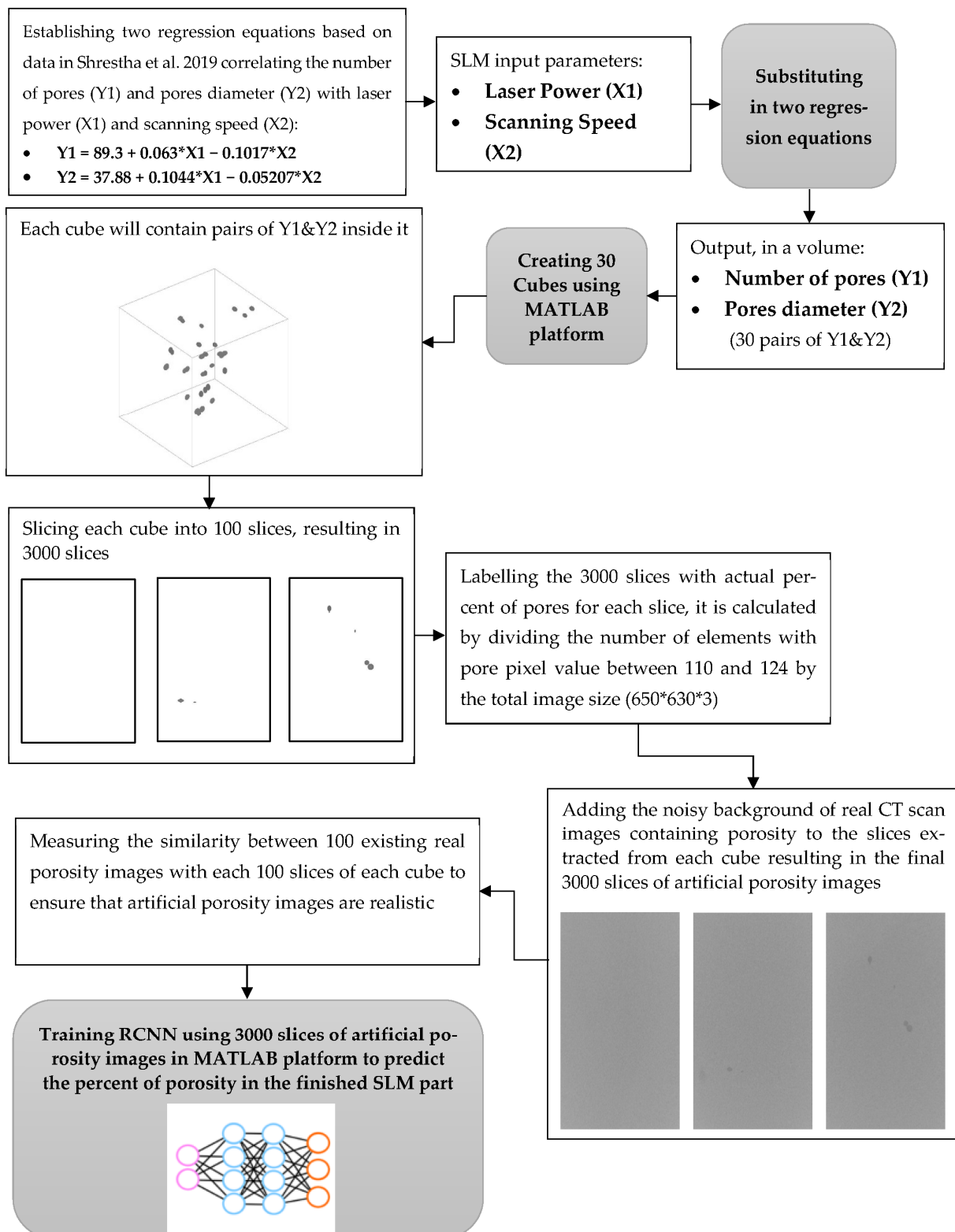


Figure 11. Flowchart for the steps of creating artificial porosity images [6].

The Minitab software was used to establish the first regression equation that fits the 24 observations [6] mentioned in the previous table, thus correlating the number of pores with the laser power and the scanning speed, which results in the following equation:

$$\text{Number of Pores} = 89.3 + 0.063 \times \text{Laser Power} - 0.1017 \times \text{Scanning Speed} \quad (1)$$

Similarly, the second regression equation was established to fit pores diameter with laser power and scanning speed data found in [6], and the dataset is shown in the following Table 3.

Table 3. Pore diameter for each laser power and scanning speed combination [6].

No.	Laser Power (W)	Scanning Speed (mm/s)	Pores Diameter (μm)
1	195	200	47
2	175	200	46
3	150	200	42
4	125	200	45
5	195	400	36
6	175	400	41
7	150	400	27
8	125	400	26
9	195	600	25
10	175	600	27
11	150	600	25

Once again, the Minitab software was used to establish the regression equation that fits the 11 observations [6] mentioned in Table 3 correlating the diameter of the pores with the laser power and the scanning speed, which results in the following equation:

$$\text{Pores Diameter} = 37.88 + 0.1044 \times \text{Laser Power} - 0.05207 \times \text{Scanning Speed} \quad (2)$$

3.2. Generating Pores Numbers and Diameters

The two regression equations established in the previous section were used to generate 30 values for the number of pores and pores diameter by substituting the 30 combinations of laser power and scanning speed found in [6]. The following is an illustrative example using a laser power of 15 W and a scanning speed of 50 mm/s:

$$\text{Number of Pores} = 89.3 + 0.063 \times (15) - 0.1017 \times (50) = 85 \text{ Pores}$$

$$\text{Pores Diameter} = 37.88 + 0.1044 \times (15) - 0.05207 \times (50) = 36.94 \mu\text{m}$$

Table 4 shows the 30 combinations of laser power and scanning speed found in [6], along with the corresponding number of pores after scaling down from a 2.6 mm^3 to a 1 mm^3 volume, the volume of the cube in which the pores will be positioned and used to train the CNN. Variations of $\pm 10 \mu\text{m}$ were applied randomly to the generated pore diameters, mimicking variations occurring in real porosity images.

Table 4. Number of pores and pores' diameter for combined laser power and scanning speed.

No.	Laser Power (W)	Scanning Speed (mm/s)	Number of Pores in 2.6 mm^3 Volume	Number of Pores after Scaling (Divided by 2.6 to Scale it to 1 mm^3 volume)	Average Pores Diameter (μm)	Maximum Pores Diameter (μm)	Minimum Pores Diameter (μm)
1	16	50	85	33	36.9469	46.9469	26.9469
2	20	50	85	33	37.3645	47.3645	27.3645
3	24	50	86	33	37.7821	47.7821	27.7821
4	32	100	81	31	36.0138	46.0138	26.0138
5	40	100	82	32	36.849	46.849	26.849
6	48	100	82	32	37.6842	47.6842	27.6842
7	48	150	77	30	35.0807	45.0807	25.0807
8	60	150	78	30	36.3335	46.3335	26.3335
9	72	150	79	30	37.5863	47.5863	27.5863

Table 4. Cont.

No.	Laser Power (W)	Scanning Speed (mm/s)	Number of Pores in 2.6 mm ³ Volume	Number of Pores after Scaling (Divided by 2.6 to Scale it to 1 mm ³ volume)	Average Pores Diameter (µm)	Maximum Pores Diameter (µm)	Minimum Pores Diameter (µm)
10	64	200	73	28	34.1476	44.1476	24.1476
11	80	200	74	28	35.818	45.818	25.818
12	96	200	75	29	37.4884	47.4884	27.4884
13	80	250	69	27	33.2145	43.2145	23.2145
14	100	250	70	27	35.3025	45.3025	25.3025
15	120	250	71	27	37.3905	47.3905	27.3905
16	96	300	65	25	32.2814	42.2814	22.2814
17	120	300	66	25	34.787	44.787	24.787
18	144	300	68	26	37.2926	47.2926	27.2926
19	112	350	61	23	31.3483	41.3483	21.3483
20	140	350	63	24	34.2715	44.2715	24.2715
21	168	350	64	25	37.1947	47.1947	27.1947
22	130	406.2	56	22	30.301166	40.301166	20.301166
23	162.5	406.2	58	22	33.694166	43.694166	23.694166
24	195	406.2	60	23	37.087166	47.087166	27.087166
25	144	450	53	20	29.4821	39.4821	19.4821
26	180	450	55	21	33.2405	43.2405	23.2405
27	156	487.5	50	19	28.782275	38.782275	18.782275
28	195	487.5	52	20	32.853875	42.853875	22.853875
29	176	550	44	17	27.6159	37.6159	17.6159
30	195	609.4	40	15	26.506542	36.506542	16.506542

3.3. Creating 3D Cubes

Overall, 30 samples of 3D cubes were created with a volume of 1 mm³ for each cube, and they contain the number of pores with diameters generated in the previous section (Table 4). Thus, the first cube has 33 pores with an average diameter of 36.94 µm. In [25], the position of pores was considered by analyzing the porosity distribution in real images of pores. They observed 975 porosity positions in X and Y. In this research, the Minitab platform was used to conduct a normality test on these observations, as shown in the following Figures 12 and 13:

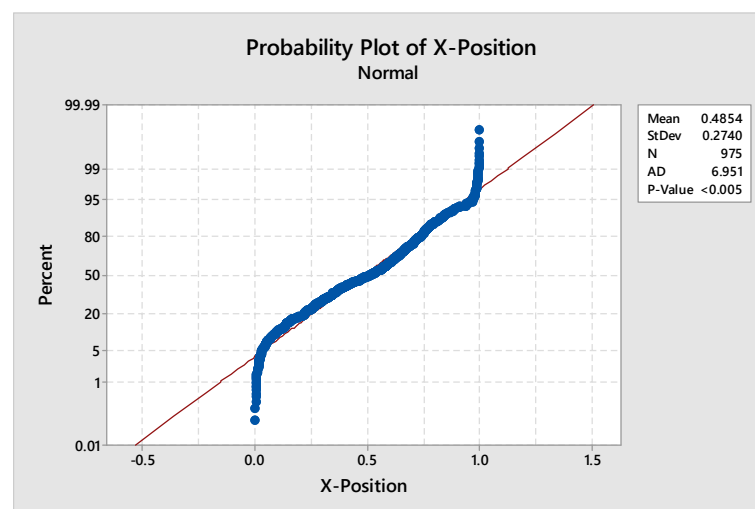


Figure 12. Probability plot for X Position.

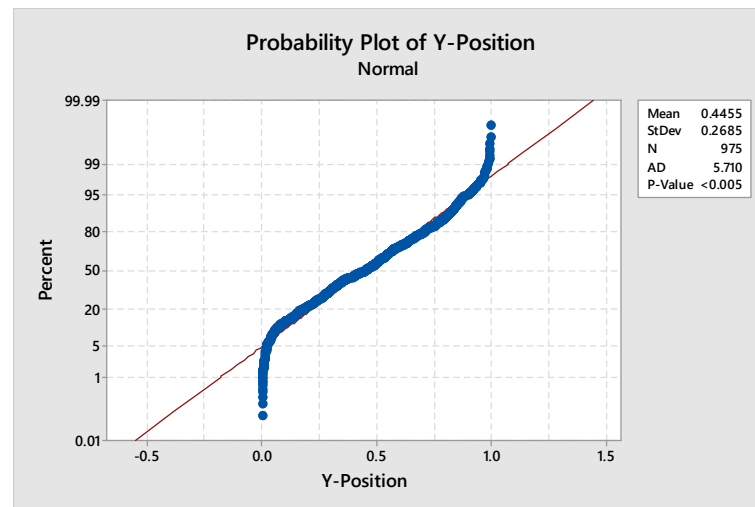


Figure 13. Probability plot for Y Position.

With a p -value of less than 0.005, the probability that these data are not coming from a normal distribution is very low, so it is concluded that the observed porosity positions are normally distributed, with a mean and a standard deviation of 0.48 and 0.27 for X-positions and 0.44 and 0.26 for Y-positions. Therefore, in this research, it was decided to produce porosity positions with the same statistical distribution, as observed in [25].

Thus, MATLAB software was used to generate normally distributed porosity positions inside each of the 30 cubes with the mean and the standard deviation mentioned previously in the X and Y positions, while the Z position was arbitrarily given the average between X and Y to produce normal distribution positions in a volume. The pores morphology was created to be similar to the 3D view of the pores shown in Figure 7 in Section 2.4.2 [6]. The following Figure 14 shows an illustrative example of the cube with 33 pores and an average diameter of 36.94 μm , as mentioned in the first combination of Table 4.

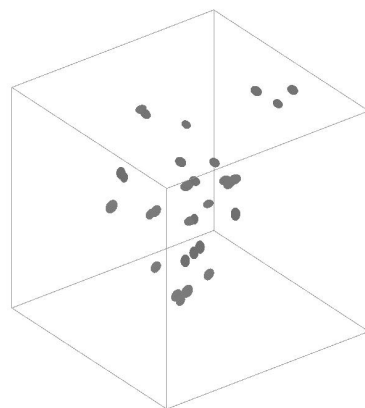


Figure 14. 3D Cube with 33 pores and average pores diameter of 36.94 μm .

3.4. Slicing 3D Cubes into 2D Images

Each cube created in the previous step was sliced using the MATLAB platform into 100 slices with a thickness of 0.01 mm, resulting in 3000 slices of 2D images, an illustrative example of the cube, and three non-sequential slices that are shown in the following Figure 15.

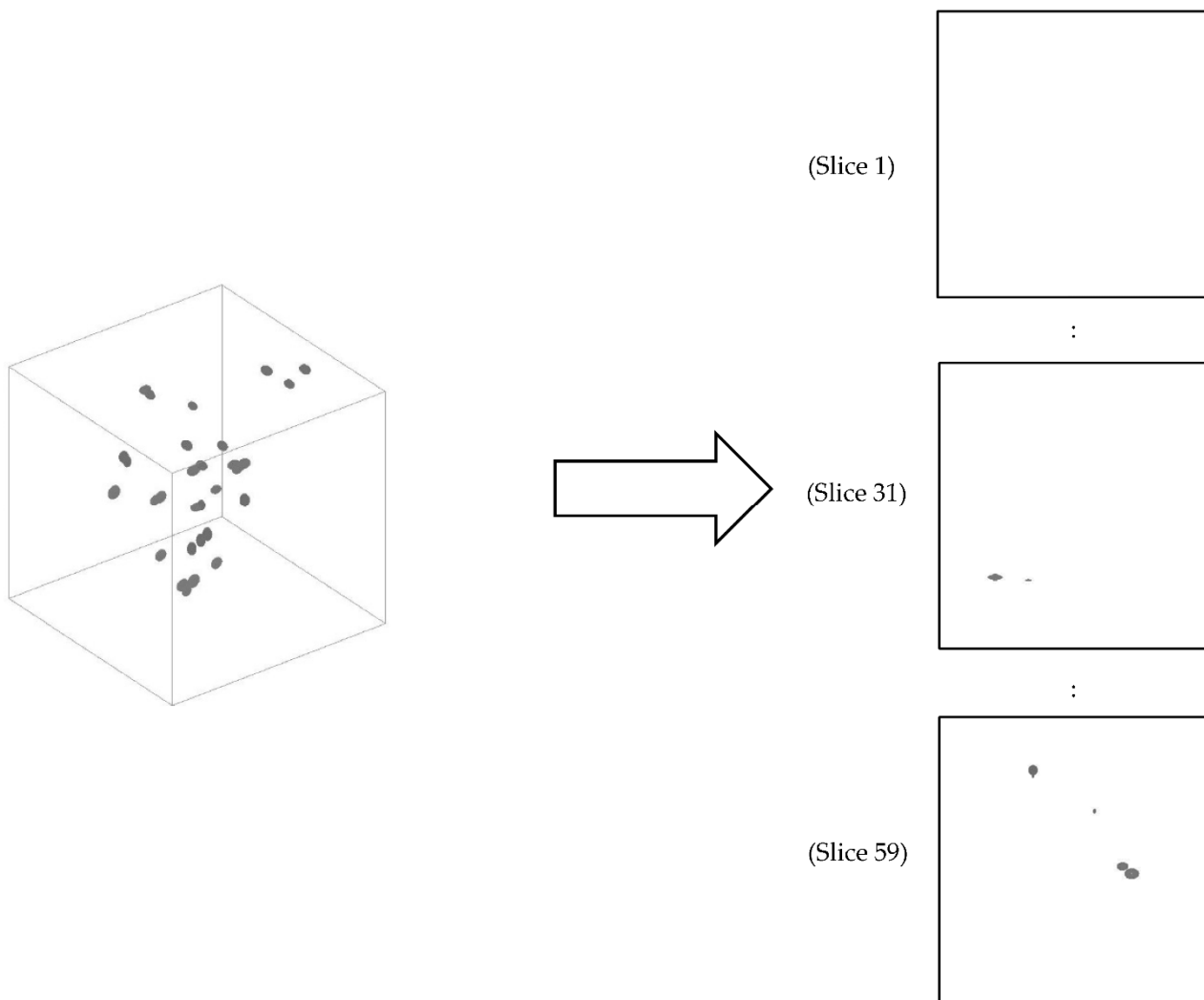


Figure 15. Illustrative example of the cube slicing.

The first slices are expected to be with no pore, as shown at the bottom of the cube. Thereafter, part of a pore is shown in some slices and parts of many pores are shown in other slices. The pore morphology tended to be near-spherical in shape, as described in Section 2.4.2 [16].

3.5. Labelling 2D Slices

The slices were labelled with the actual percent of porosity for each slice using MATLAB software, and were calculated by dividing the number of elements with specific pore unique pixel values by the total image size ($650 \times 630 \times 3$). The pixel values for the pores were determined by inspecting the pixel values of porosity seen in real CT Scan images [26], and are between 110 and 124. The first slice has no elements with a pixel value in the range between 110 and 124 so the actual percentage of pore is 0. In slice 31 there are 258 elements with pixel values in the range specified, so the actual percent of pore is $(258 / (650 \times 630 \times 3)) \times 100 = 0.0210$, similarly for slice 59 with 2193 elements of pixel values between 110 and 124, the actual percent of pore is $(2193 / (650 \times 630 \times 3)) \times 100 = 0.1785$, and the average actual percent of pore for 3000 slices is 0.0134.

3.6. Adding Noisy Background

Firstly, image processing in the MATLAB platform was conducted to fuse the noisy background of 100 CT scan images containing porosities with the slices extracted from each

cube, resulting in the first version of the filtered artificial images shown in the following Figure 16.

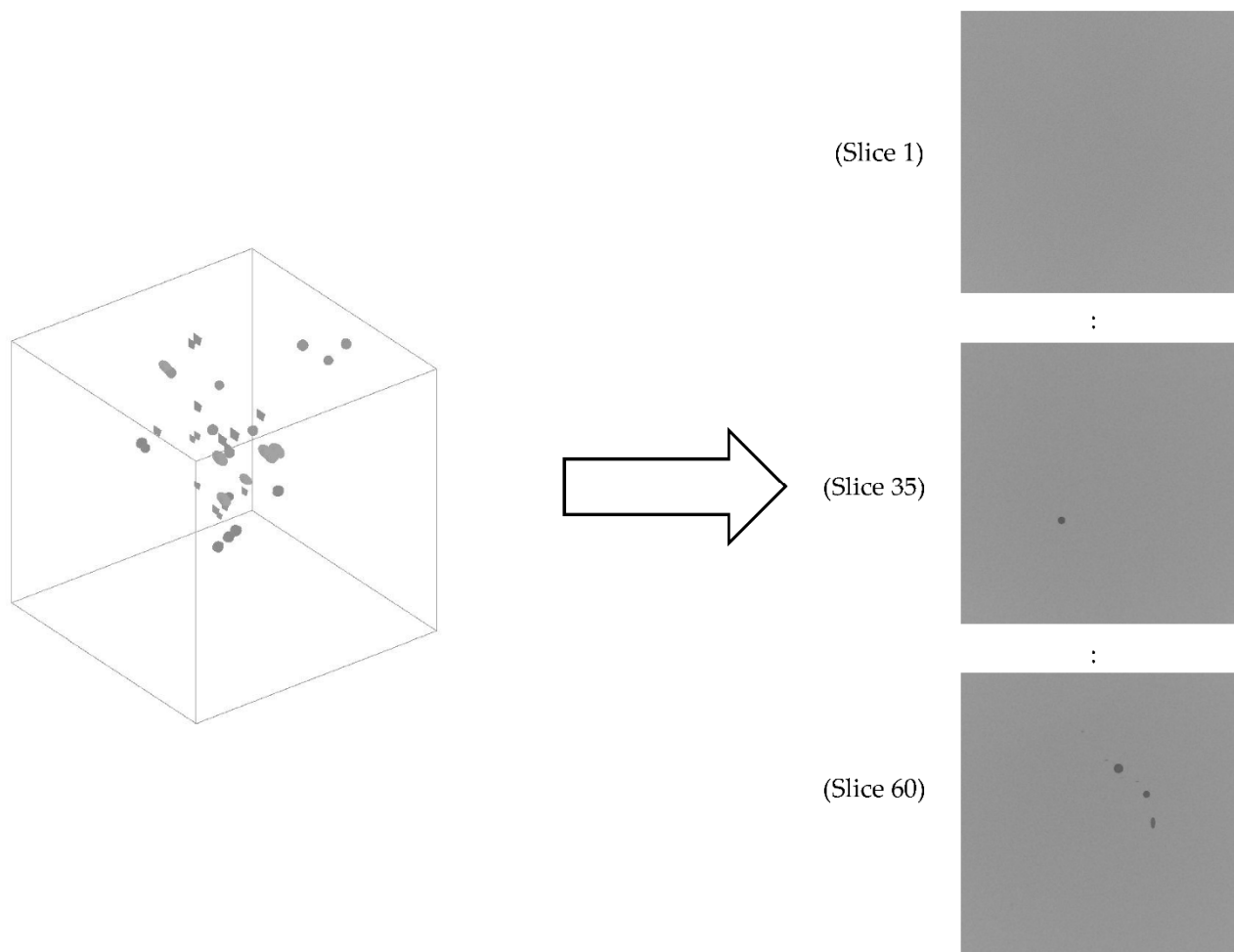


Figure 16. Illustrative example of the first version of artificial porosity images.

Secondly, in the artificial images, the edges of the pores have a uniform shading, making them clearly distinguishable from the background. This is not a true representation of porosity seen on real CT scans, where shade variations make it difficult to properly distinguish pores' edges. Thus, in a second version, image processing in the MATLAB platform was conducted to further filter the artificial porosity images by creating similar noise, so the background of a sample of 100 existing images was inserted into 100 pores slices extracted from 3D cube after reducing the pixel value for its white background from 255 to 155 to convert it to a gray background. The artificial images were overlaid with the noisy background of real images. The degree of overlaying was determined by a factor (between 0 and 1) following the method described in [27].

Thus, with a factor of 1, the pore image will be shown without noisy background and with a factor of 0, and the noisy background will be shown without pores. After many trial and error experiments, a factor of 0.125 was considered to visually be the best value that combined both pore and noisy background images, as shown in the following Figure 17.

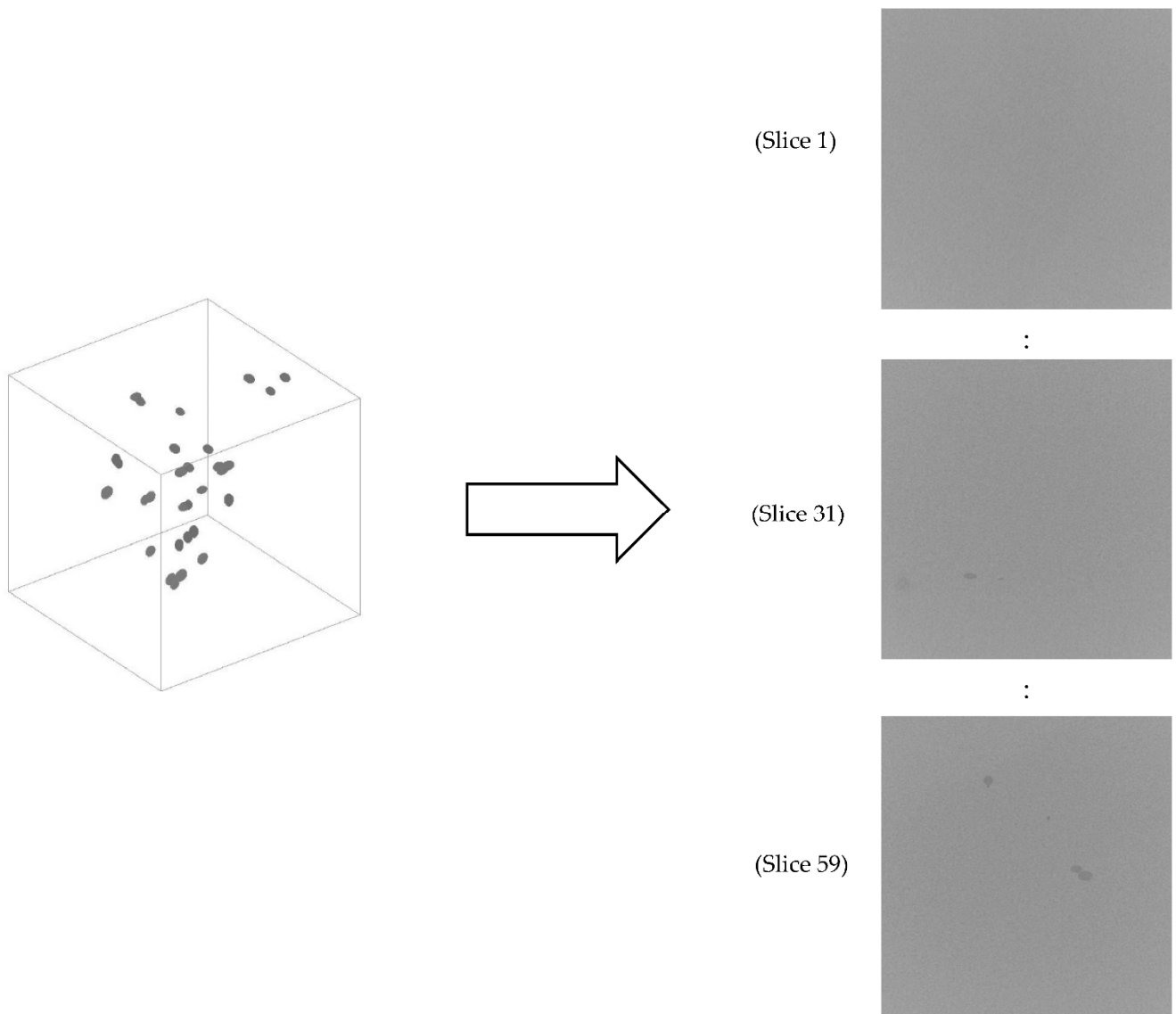


Figure 17. Illustrative example of the final version of artificial porosity images.

As shown in the slices, the noise in the background and the pores appear more like real porosity images as the edges are not as clearly defined, but this is a subjective evaluation. The following Section 3.7 will present quantitative measure for the similarity between real and artificial porosity images to ensure that the artificial images are realistic.

3.7. Measuring the Similarity between Artificial and Real Porosity Images

The created artificial porosity images were compared with real CT scan slices of finished SLM parts [26] to verify that the simulated images are close to reality. The real images are only used as a demonstration and are not directly linked with the pore formation equations mentioned in Section 3.1. The following Figure 18 shows an illustrative example of the slices before and after processing, which was required to focus on the bulk of the material and to obtain images of the same size as the artificial images.

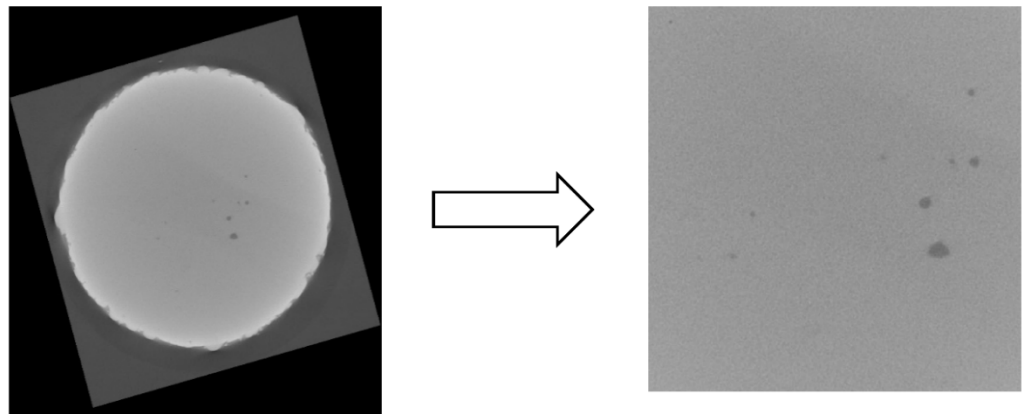


Figure 18. Illustrative example of the real existing porosity images [26].

Figure 19 presents the real image along with the first version of the artificial image.

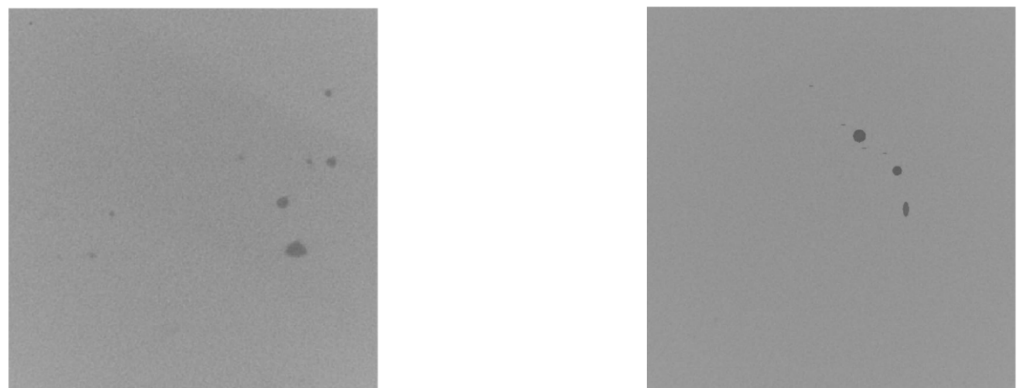


Figure 19. Real image (Left) vs. first version of artificial image (Right).

Samples of 100 slices of real images were taken and compared with each of the first versions of 100 artificial images created in the previous section. The comparison was made using a quantitative method called Structural Similarity Index (SSI). It is a measure that assesses the images based on three computational terms, namely the luminance (l), the contrast (c), and the structural terms (s). Multiplying the three terms results in the overall index. If two images are exactly the same, the index should be 1, and if they are totally different the index should be close to zero. The mathematical equations for calculating SSI for images x and y are as follow [28]:

$$SSI(x,y) = [l(x,y)]^\alpha \times [c(x,y)]^\beta \times [s(x,y)]^\gamma \tag{3}$$

where:

$$l(x,y) = (2 \times \mu_x \times \mu_y + C1) / (\mu_x^2 + \mu_y^2 + C1) \tag{4}$$

$$c(x,y) = (2 \times \sigma_x \times \sigma_y + C2) / (\sigma_x^2 + \sigma_y^2 + C2) \tag{5}$$

$$s(x,y) = (\sigma_{xy} + C3) / (\sigma_x \times \sigma_y + C3) \tag{6}$$

μ_x and μ_y are local means, σ_x and σ_y are standard deviations, and σ_{xy} is cross-covariance for images x and y. The exponents for luminance, contrast and structural are alpha(α), beta(β), and gamma(γ), while C1, C2, and C3 are constants added to avoid instability for image regions with local mean or standard deviation close to zero.

MATLAB software was used to calculate SSI between the real and first version of artificial porosity images, the average similarity index for 3000 slices was 0.9586. The same

100 samples of real images were used to compare them, with the final version of artificial porosity images shown in the following Figure 20:

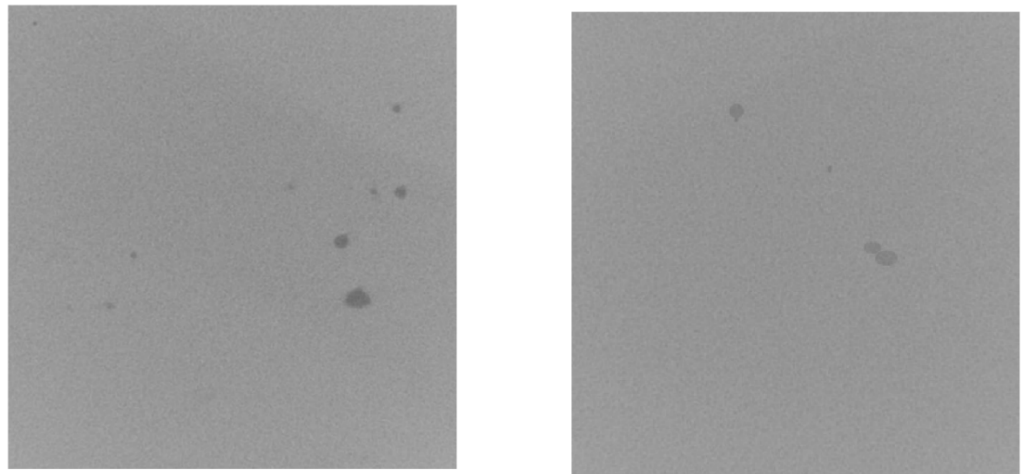


Figure 20. Real image (Left) vs. final version of artificial image (Right).

The average similarity index for 3000 slices was improved to 0.9967, which means that the final version of artificial porosity images mimics better real images since the index is closer to 1.

3.8. Study Limitations

The created artificial porosity images in this section will be used only to test the proposed CNN algorithms that will be developed in Section 4. The study did not aim to study the porosities in depth, so no experiments have been conducted, but the paper proposes a method that will enhance such studies, particularly in predicting the percent of porosity as will be demonstrated in Section 4. In the future, real experiments can be conducted in order to produce real porosity images.

4. Predicting the Porosity in Selective Laser Melting Parts

Using the artificial images created in Section 3, this section will show three methods for predicting the percentage of porosity in SLM parts. The first one is the existing image binarization method, which is one of the main methods for measuring porosity along with the Archimedes method [22]. Archimedes' principle might be used in the case of producing real SLM parts, and this paper uses artificial porosity images, so the image binarization method will be conducted and explained in Section 4.1. The second and third methods are Regression Convolutional Neural Network (RCNN) and hybrid Bees Regression Convolutional Neural Network (BA-RCNN), which will be explained in detail in Section 4.2.

4.1. Predicting the Porosity Using Image Binarization

There is a problem related to accurately assessing the porosity in SLM parts [21]. The problem is the difficulty and subjectivity in selecting an appropriate grayscale threshold for binary image conversion to highlight defective regions and determine the true level of porosity, as mentioned previously in Section 2.5.

The first version of created artificial images presented in the previous section were binarized using an adaptive thresholding algorithm provided in the MATLAB platform, which selects the threshold based on local mean intensity in the pixel neighborhood, and is determined by a sensitivity factor, between 0 and 1, that indicates the sensitivity toward thresholding more pixels as a foreground [29]. This sensitivity factor is selected manually. The following Figure 21 shows the first version of the artificial image, along with the binarized image with an arbitrarily selected sensitivity factor of 0.66.

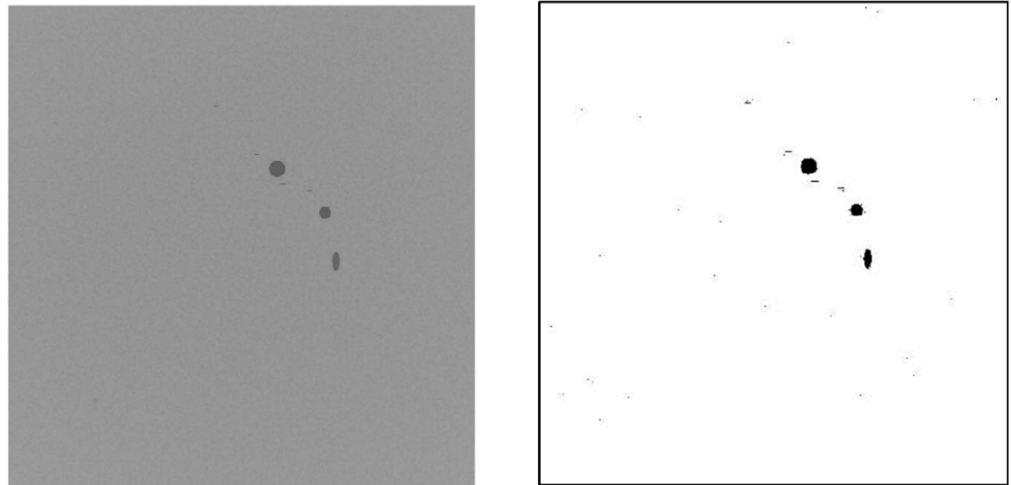


Figure 21. First version of artificial image (Left) vs. binarized artificial image (Right).

As can be seen in the figure, there are tiny undesired black spots in different positions in the binarized image, and the undesired spots also appear in slices with no pores, as shown in the following Figure 22.

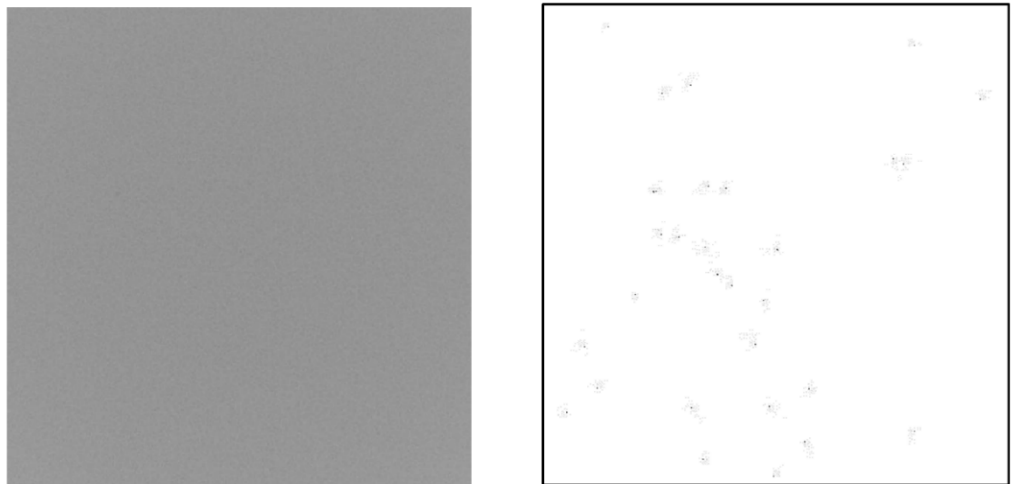


Figure 22. First version of artificial image with no pore (Left) vs. binarized artificial image (Right).

The average actual percent of pore for 3000 slices was 0.0134, while the average percent of pore for 3000 binarized images is overestimated with a value of 0.0578, so the absolute error is 0.0444. The prediction accuracy with a difference of less than a threshold of 0.02 (percent of observations with error less than 0.02) is 64.47%.

The same approach was followed for the final version of artificial porosity images, and the following Figure 23 shows the artificial image along with the binarized image, with a sensitivity factor of 0.66.

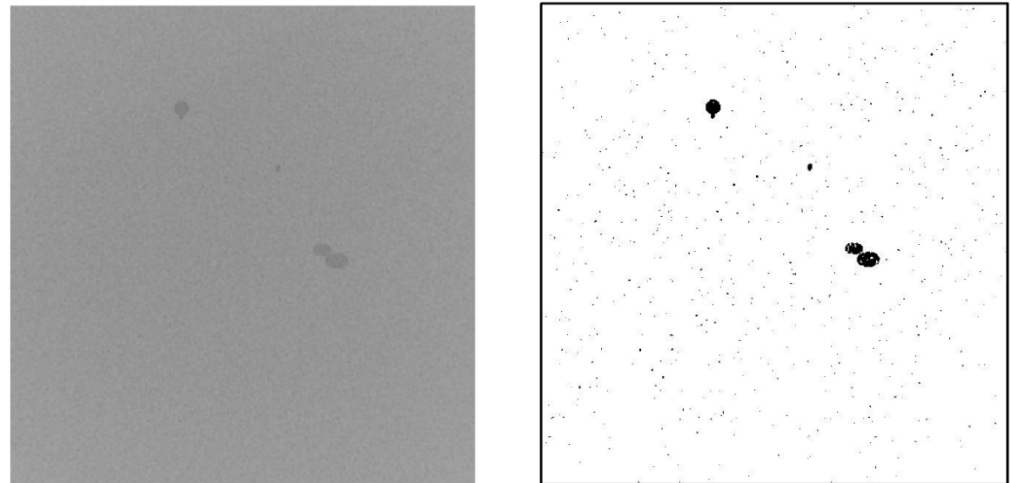


Figure 23. Final version of artificial image (Left) vs. binarized artificial image (Right).

As can be seen in the figure, there are tiny undesired black spots in different positions in the binarized image, confirming the problem stated in [21], which is a result of inconsistent grayscale in CT scan slices because of the mutual influence of CT setup and radiodensity variation. Removing these spots using image processing is time-consuming since they appear in different positions in each slice without a simple pattern, so the processing needs to be performed image by image to distinguish between the undesired black spots and the pores first. Following that, unwanted spots need to be replaced with a white background because they are counted in the porosity calculation which overestimates the percent of porosity. Such an issue also occurs in the pores, as tiny white spots would alter their morphological feature and slightly reduce the percentage of porosity. However, the effect of this on porosity calculations is negligible when compared to the effect of the small black spots occurring in the large background. Depending on the sensitivity factor used, the black spots also appear in slices with no pores, as shown in the following Figure 24.

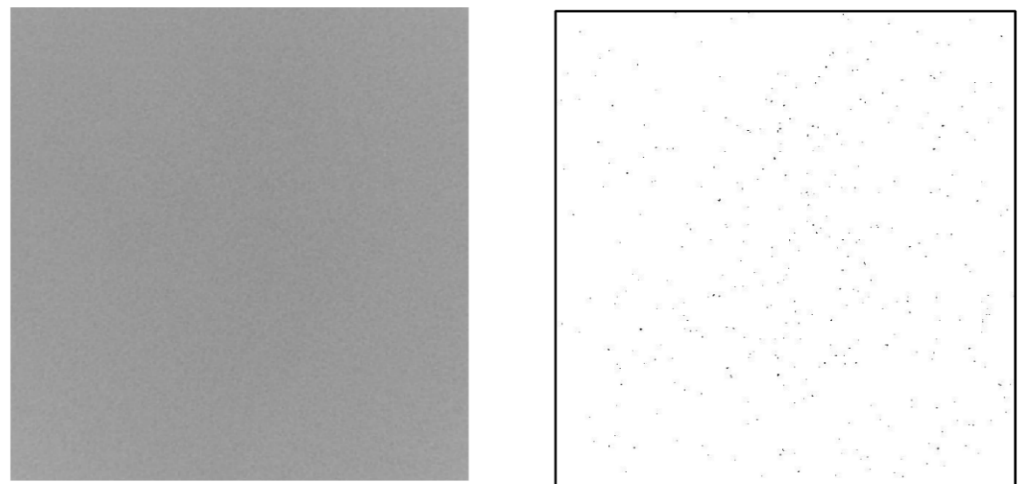


Figure 24. Final version of artificial image with no pore (Left) vs. binarized artificial image (Right).

Experimenting with different sensitivity factors between 0.63 to 0.74 resulted in the following binary images with different percentages of porosity as shown in Figure 25.

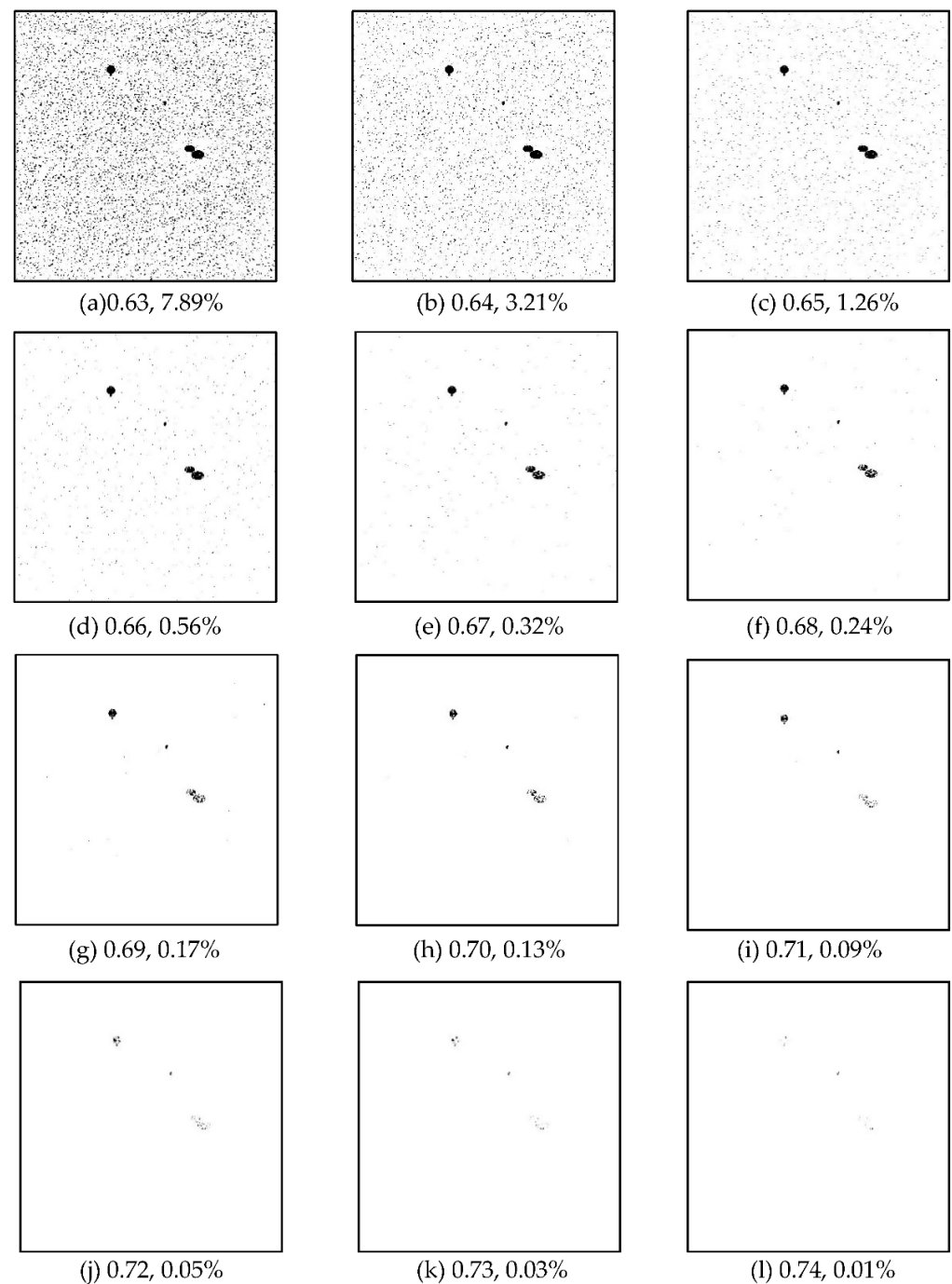


Figure 25. Binary images with different sensitivity factors and percent of porosity.

As can be seen from the images, increasing the sensitivity factors reduces the black spots resulting from the noisy background, but it alters the pore's morphological features dramatically. A sensitivity factor of 0.69 seems relatively better and it will be selected to binarize all 3000 slices since it yielded the most accurate percent of porosity of 0.17%, which is close to the actual percent of pore for the original slice with a value of 0.1785%. It is worth noting that in the case of producing real porosity images, sensitivity factor selection will be subjective and difficult since the actual percentage of porosity will be unknown. The average percent of pore for 3000 slices was 0.0203, while the average percent of pore for 3000 binarized images is overestimated with a value of 0.0424, so the absolute error is 0.0221. The prediction accuracy with a difference less than a threshold of 0.02 (percent of observations with error less than 0.02) is 68.60%.

4.2. Predicting the Porosity Using RCNN and BA-RCNN

CNN can be used for regression problems to predict numerical values based on images, so regression CNN will be used to predict the percent of porosity based on created artificial porosity images in the previous section. As mentioned previously (in Section 3.5), the images were labelled using the actual percent of porosity calculated during the creation process by dividing the number of elements with specific pore unique pixel values by the total image size. CNN learns the porosity pattern in artificial porosity images that mimic CT scan images of the finished SLM part and predict the percent of porosity without the need for subjective difficult thresholding determination to convert the single slice to a binary image, which ultimately achieves automatized quality assessment.

4.2.1. RCNN and BA-RCNN Architecture

The CNN architecture for predicting the percent of porosity is composed of 22 layers with one input layer, five convolutional layers, five rectified linear unit layers, five batch normalization layers, four average pooling layers, one fully connected layer, and one regression layer.

The input layer is represented by a matrix with height by width size (650×630). It contains pixel brightness values between 0 for black regions to 255 for white regions. The convolutional layers contain filters represented by weight matrix slide along the pixel brightness matrix using a special dot product to create a feature map matrix [30]. The rectified linear unit layer comes after each convolutional layer to increase the effectiveness and speed of the training by maintaining positive values and mapping negative values to zero [31]. In addition, the batch normalization layer comes after each convolutional layer as a supplement layer mitigating the overfitting risk [32]. Pooling layers are used between the convolutional layers for output dimensionality reduction [33] without losing the important image features, which helps in minimizing the computational time. Regression and fully connected layers are the output layers that show the predicted percentage of pores.

The normal number of convolutional layers to start is between two to three layers with a filter size of 3×3 or 5×5 as advised in [31], CNN was designed with five convolutional layers with four average pooling layers in between, with the number of filters ranging between 8 for the first layer and 128 for the last one. Each layer has twice the number of filters of the previous layer [34]. The filter size is 5×5 , the section depth is 3, and the padding that detects the image edges is set as 'same', so the padding size is automatically calculated at the training time, producing output size equivalent to input size when the stride (number of pixel shift) is one.

The pooling type is 'average' which takes the average presence of the feature, while the max pooling layer takes the most activated feature, so the average pooling is used with light background and max pooling is better with dark background [35], the default size of pooling layer is 2×2 [30], but it yielded high computational cost since the image input size is big (650×630). The size was changed to 4×4 with a stride value of 4 to minimize the training time.

CNN was trained using SGDM, which is the most common training algorithm [32]. The default values for this algorithm are an initial learning rate of 0.01, a momentum of 0.9, a regularization of 1×10^{-4} , and the maximum number of epochs is 20, as presented in [36]. After applying some experiments and monitoring the validation accuracy, the momentum was changed to 0.8, and with regularization became 1×10^{-10} .

The RCNN algorithm will train the artificial porosity images of the SLM part to predict the percent of porosity without the need for subjective difficult threshold determination to convert the single slice to a binary image, as mentioned in [21].

The hybrid algorithm (BA-RCNN) uses BA to optimize the parameter values for section depth that controls the network depth, the initial learning rate that is used for features learning, the momentum that performs the hyperparameters update and regularization that prevents overfitting [37] to reach the minimum prediction error on the validation set.

The BA consists of global and local searches. The global search is done by the scout bees that evaluate random positions based on the fitness value. In the local search, the best sites are selected, and the remaining sites are abandoned. The intense search is done to select the elite sites, which are the best among the best sites selected in the local search. The next step is recruiting more bees for the elite sites based on the size of the neighborhood search space and recruiting lower bees for other sites to conduct the local search [38]. The stopping conditions for this iterative process are:

- Finding the optimal solution
- Exceeding the iteration number
- No improvement over specified sequential iterations

The values of BA hyperparameters are assigned based on the capability of the computer and equations in [39]:

- Scout bees (n) = 4
- Selected bees (m) = $0.5 \times n = 2$
- Elite bees (e) = 1
- Recruited bees for e (nep) = $2 \times m = 4$
- Recruited bees for other best sites (nsp) = $0.5 \times n = 2$
- Neighborhood size (ngh) = $0.1 \times (\text{Maximum} - \text{Minimum})$:
 - **Section Depth:** $0.1 \times (3 - 1) = 0.1 \times 2 = 0.2$
 - **Initial Learning Rate:** $0.1 \times (1 - 1 \times 10^{-2}) = 0.1 \times 0.99 = 0.099$
 - **Momentum:** $0.1 \times (0.98 - 0.8) = 0.1 \times 0.18 = 0.018$
 - **Regularization:** $0.1 \times (1 \times 10^{-2} - 1 \times 10^{-10}) = 0.1 \times 0.01 = 0.001$

The following Figure 26 shows the pseudo-code for the BA-RCNN algorithm:

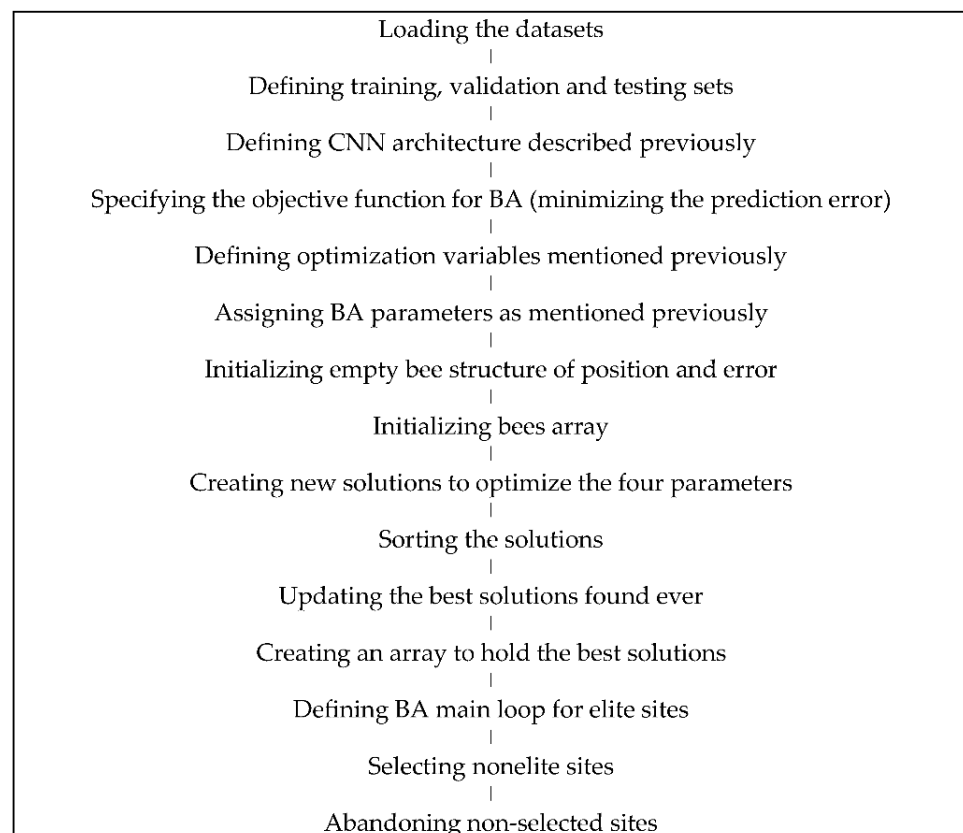


Figure 26. The pseudo code for BA-RCNN.

The following Figure 27 summarizes the task for hybrid regression CNN:

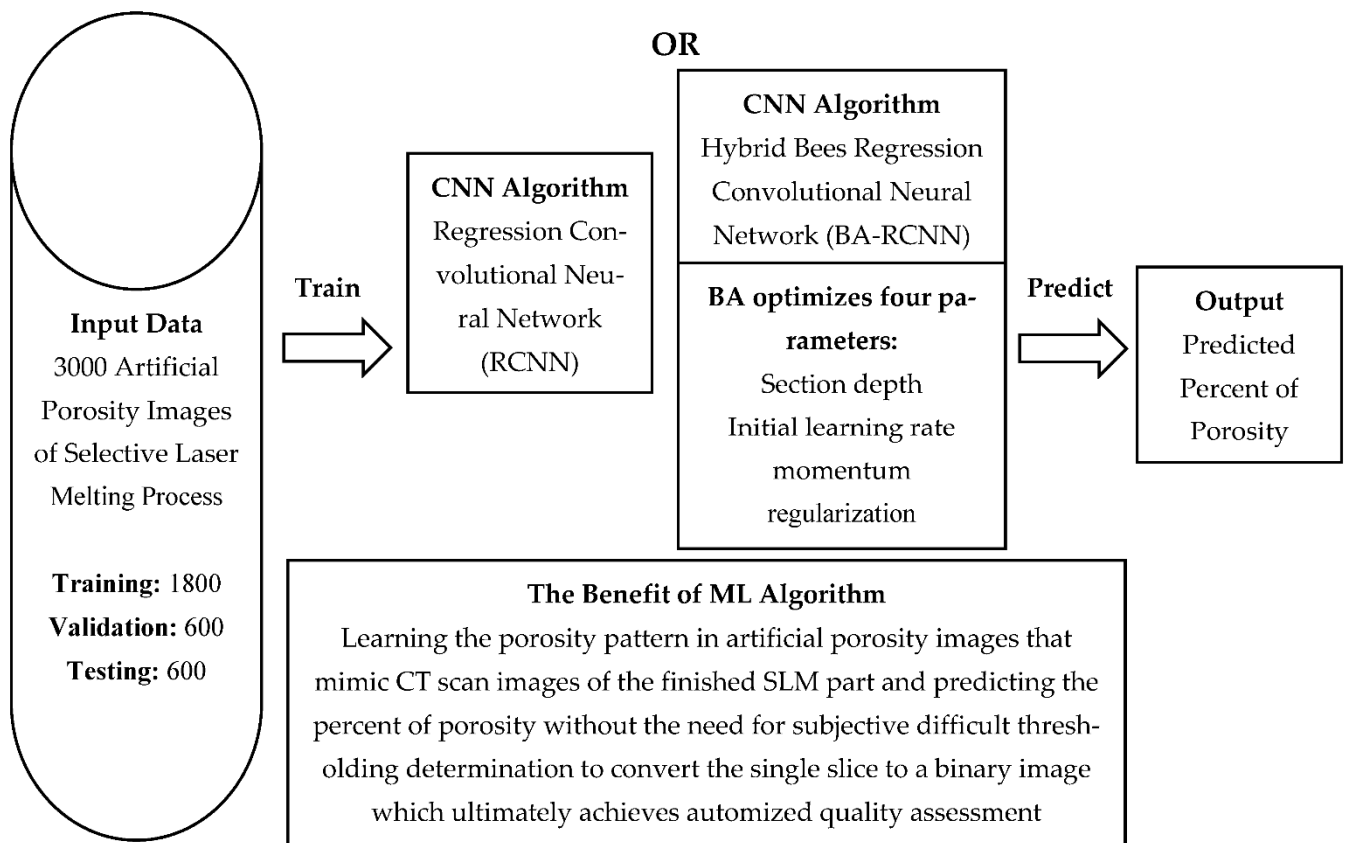


Figure 27. Illustrative diagram for hybrid regression CNN.

4.2.2. RCNN and BA-RCNN Results

MATLAB is the platform used to apply RCNN and BA-RCNN on the newly created 3000 artificial porosity images, of which 1800 images are for training and 600 are for each of the validation and testing sets to predict the percent of porosity without the need for subjective difficult thresholding determination to convert the single slice to a binary image, which ultimately achieves automated quality assessment. The following Table 5 shows the average percent of porosity error (the difference between the actual and predicted percent of porosity on average) for the first version of artificial porosity images.

Table 5. Average percent of porosity error (first version).

	Original RCNN	Hybrid BA-RCNN
Average Percent of Porosity Error in Training Set	0.0164	0.0169
Average Percent of Porosity Error in Validation Set	0.0171	0.0160
Average Percent of Porosity Error in Testing Set	0.0189	0.0191

The minimum percent of porosity error value of 0.0160 comes with the validation set in BA-RCNN, and the following Table 6 shows the optimal CNN parameters values optimized using BA.

Table 6. Optimal CNN parameters values using BA (first version).

	Value
Optimal Section Depth	3
Optimal Initial Learning Rate	0.0118
Optimal Momentum	0.8229
Optimal Regularization	0.0091
Validation Error	0.0160

The minimum error value of 0.0160 was achieved with a section depth of 3, 0.0118 initial learning rate, a momentum value of 0.8229, and a regularization parameter of 0.0091, which is less than the error value of 0.0444 for the image binarization method. The following Table 7 shows the prediction accuracy with a difference less than a threshold of 0.02 (percent of observations with error less than 0.02) for all three sets, along with computational time for all algorithms.

Table 7. Prediction accuracy and computational time for algorithms (first version).

	Original RCNN	Hybrid BA-RCNN
Training Accuracy	81.22%	82.06%
Validation Accuracy	81.50%	81.67%
Testing Accuracy	78.83%	80.67%
Computational Time	18 min 17 s	18 min 13 s

The existing original RCNN produced 78.83% prediction accuracy in the testing set, which is approximately 14% better than the accuracy resulting from the image binarization method with a value of 64.47%. The novel hybrid BA-RCNN produced better prediction accuracy in all training, validation, and testing sets, which means it has better generalization capability than RCNN. The accuracy in the testing set has a value of 80.67%, which is approximately 16% better than the existing image binarization method, and the computational time is almost similar in both algorithms. The following Table 8 shows the prediction accuracy for all three methods.

Table 8. Porosity prediction accuracy (first version).

	Image Binarization	Original RCNN	Hybrid BA-RCNN
Porosity Prediction Accuracy	64.47%	78.83%	80.67%

The same approach is followed to predict the percent of porosity for the final version of artificial porosity images. The following Table 9 shows the average percent of porosity error (the difference between the actual and predicted percent of porosity on average) for the first version of artificial porosity images.

Table 9. Average percent of porosity error (final version).

	Original RCNN	Hybrid BA-RCNN
Average Percent of Porosity Error in Training Set	0.0229	0.0230
Average Percent of Porosity Error in Validation Set	0.0231	0.0214
Average Percent of Porosity Error in Testing Set	0.0236	0.0234

The minimum percent of porosity error value of 0.0214 comes with the validation set in BA-RCNN, and the following Table 10 shows the optimal CNN parameters values optimized using BA.

Table 10. Optimal CNN parameters values using BA (final version).

	Value
Optimal Section Depth	1
Optimal Initial Learning Rate	0.0101
Optimal Momentum	0.9568
Optimal Regularization	0.0097
Validation Error	0.0214

The minimum error value of 0.0214 comes with a section depth of 1, 0.0101 initial learning rate, a momentum parameter of 0.9568, and a regularization value of 0.0097, and is less than the error value of 0.3167 for the image binarization method. The following Table 11 shows prediction accuracy for training, validation, and testing sets with a difference less than a threshold of 0.02 (percent of observations with error less than 0.02), along with computational time for best iteration for all algorithms.

Table 11. Prediction accuracy and computational time for algorithms (final version).

	Original RCNN	Hybrid BA-RCNN
Training Accuracy	74.94%	85.94%
Validation Accuracy	76%	87.33%
Testing Accuracy	75.50%	85.33%
Computational Time	15 min 43 s	13 min 40 s

The existing original RCNN produced 75.50% prediction accuracy in the testing set, which is approximately 7% better than the accuracy resulting from the image binarization method with a value of 68.60%. The novel hybrid BA-RCNN produced better prediction accuracy in all training, validation, and testing sets, which means it has better generalization capability than RCNN. The accuracy in the testing set has a value of 85.33% which is approximately 17% better than the existing image binarization method, and the hybrid BA-RCNN is cost-effective since the computational time is reduced by approximately 2 min. The following Table 12 shows the prediction accuracy for all three methods.

Table 12. Porosity average prediction accuracy (final version).

	Image Binarization	Original RCNN	Hybrid BA-RCNN
Porosity Prediction Accuracy	68.60%	75.50%	85.33%

The contribution of the paper is developing a new approach based on the use of a Regression Convolutional Neural Network (RCNN) algorithm to predict the percent of porosity in CT scans of finished SLM parts, without the need for subjective difficult thresholding determination to convert a single slice to a binary image, the model achieved better prediction accuracy than the existing image binarization method by 17%. In order to test the algorithm, as the training of the RCNN would require a large amount of experimental data, artificial porosity images mimicking real CT scan slices of the finished SLM part were created with a similarity index of 0.9976 with real images.

5. Conclusions

Assessing the porosity in Selective Laser Melting (SLM) parts is a challenging issue, and the drawback of using the existing gray value analysis method to assess the porosity is

the difficulty and subjectivity in selecting a uniform grayscale threshold for binary image conversion to detect the porosity. This paper demonstrated a new efficient approach of creating artificial porosity images, mimicking real CT scan slices of finished SLM part with a similarity index of 0.9976 which can be used to train an accurate Regression Convolutional Neural Network (RCNN) for automatic porosity prediction. Further work is required to tune this approach for the creation of artificial images mimicking a wider range of porosity types, and experiments need to be performed to do so. The MATLAB platform was used to develop the RCNN. In order to predict the percent of porosity in the created artificial porosity images, it improved porosity prediction accuracy from 68.60% for image binarization method to 75.50% for RCNN. The algorithm was further developed by optimizing its parameters the using Bees Algorithm (BA), which mimics the behavior of honeybees, with the hybrid Bees Regression Convolutional Neural Network (BA-RCNN) producing better prediction accuracy with a value of 85.33%.

Author Contributions: Conceptualization, N.M.H.A., M.P. and S.B.; methodology, N.M.H.A., M.P. and S.B.; software, N.M.H.A.; validation, N.M.H.A., M.P. and S.B.; formal analysis, N.M.H.A., M.P. and S.B.; investigation, N.M.H.A., M.P. and S.B.; resources, N.M.H.A., M.P. and S.B.; data curation, N.M.H.A., M.P. and S.B.; writing—original draft preparation, N.M.H.A.; writing—review and editing, M.P. and S.B.; visualization, N.M.H.A., M.P. and S.B.; supervision, M.P. and S.B.; project administration, N.M.H.A., M.P. and S.B.; funding acquisition, N.M.H.A., M.P. and S.B. All authors have read and agreed to the published version of the manuscript.

Funding: This research received no external funding.

Institutional Review Board Statement: Not applicable.

Informed Consent Statement: Not applicable.

Data Availability Statement: Not applicable.

Acknowledgments: This research was supported by the project Additive Manufacturing using Metal Pilot Line (MANUELA), which received funding from the European Union’s Horizon2020 research and innovation programme under grant agreement No. 820774.

Conflicts of Interest: The authors declare no conflict of interest.

References

1. ISO/ASTM 52900:2021; Additive Manufacturing. General Principles. Fundamentals and Vocabulary. Available online: <https://www.iso.org/obp/ui/#iso:std:iso-astm:52900:ed-2:v1:en> (accessed on 15 November 2022).
2. Farinia Group. What Is Additive Layer Manufacturing (ALM)? Available online: <https://www.farinia.com/additive-manufacturing/3d-technique/additive-layer-manufacturing> (accessed on 4 January 2020).
3. Lastra, R.; Pereira, A.; Diaz-Cacho, M.; Acevedo, J.; Collazo, A. Spare Parts Made by Additive Manufacturing to Improve Preventive Maintenance. *Appl. Sci.* **2022**, *12*, 10564. [CrossRef]
4. Abdulhameed, O.; Al-Ahmari, A.; Ameen, W.; Mian, S.H. Additive manufacturing: Challenges, trends, and applications. *Adv. Mech. Eng.* **2019**, *11*, 1687814018822880. [CrossRef]
5. Metal, A.M. Applications for Metal Additive Manufacturing Technology. Available online: <https://www.metal-am.com/introduction-to-metal-additive-manufacturing-and-3d-printing/applications-for-additive-manufacturing-technology/> (accessed on 10 January 2020).
6. Shrestha, S.; Starr, T.; Chou, K. A study of keyhole porosity in selective laser melting: Single-track scanning with micro-CT analysis. *J. Manuf. Sci. Eng.* **2019**, *141*, 71004. [CrossRef]
7. Snell, R.; Tammam-Williams, S.; Chechik, L.; Lyle, A.; Hernández-Nava, E.; Boig, C.; Panoutsos, G.; Todd, I. Methods for rapid pore classification in metal additive manufacturing. *JOM* **2020**, *72*, 101–109. [CrossRef]
8. Li, B.H.; Hou, B.C.; Yu, W.T.; Lu, X.B.; Yang, C.W. Applications of artificial intelligence in intelligent manufacturing: A review. *Front. Inf. Technol. Electron. Eng.* **2017**, *18*, 86–96. [CrossRef]
9. De Filippis, L.A.C.; Serio, L.M.; Facchini, F.; Mummolo, G. ANN Modelling to Optimize Manufacturing Process. In *Advanced Applications for Artificial Neural Networks*; IntechOpen: London, UK, 2017.
10. Wuest, T.; Weimer, D.; Irgens, C.; Thoben, K.D. Machine learning in manufacturing: Advantages, challenges, and applications. *Prod. Manuf. Res.* **2016**, *4*, 23–45. [CrossRef]
11. Singh, A.K.; Ganapathysubramanian, B.; Sarkar, S.; Singh, A. Deep learning for plant stress phenotyping: Trends and future perspectives. *Trends Plant Sci.* **2018**, *23*, 883–898. [CrossRef] [PubMed]

12. Alamri, N.M.H.; Packianather, M.; Bigot, S. Deep learning: Parameter optimization using proposed novel hybrid bees Bayesian convolutional neural network. In *Applied Artificial Intelligence*; Taylor & Francis: Milton Park, UK, 2022; pp. 1–26.
13. Sun, S.; Brandt, M.; Easton, M. Powder bed fusion processes: An overview. In *Laser Additive Manufacturing*; Elsevier: Amsterdam, The Netherlands, 2017; pp. 55–77.
14. Bauer, T. Prediction of Process Parameters in Selective Laser Melting. Ph.D. Thesis, ETH Zurich, Zürich, Switzerland, 2021.
15. Gu, D.; Ma, C.; Xia, M.; Dai, D.; Shi, Q. A multiscale understanding of the thermodynamic and kinetic mechanisms of laser additive manufacturing. *Engineering* **2017**, *3*, 675–684. [[CrossRef](#)]
16. Tan, Q.; Liu, Y.; Fan, Z.; Zhang, J.; Yin, Y.; Zhang, M.X. Effect of processing parameters on the densification of an additively manufactured 2024 Al alloy. *J. Mater. Sci. Technol.* **2020**, *58*, 34–45. [[CrossRef](#)]
17. Kim, H.; Lin, Y.; Tseng, T.L.B. A review on quality control in additive manufacturing. *Rapid Prototyp. J.* **2018**, *24*, 645–669. [[CrossRef](#)]
18. Zhang, B.; Liu, S.; Shin, Y.C. In-Process monitoring of porosity during laser additive manufacturing process. *Addit. Manuf.* **2019**, *28*, 497–505. [[CrossRef](#)]
19. Coeck, S.; Bisht, M.; Plas, J.; Verbist, F. Prediction of lack of fusion porosity in selective laser melting based on melt pool monitoring data. *Addit. Manuf.* **2019**, *25*, 347–356. [[CrossRef](#)]
20. Wang, C.; Tan, X.P.; Tor, S.B.; Lim, C.S. Machine learning in additive manufacturing: State-of-the-art and perspectives. *Addit. Manuf.* **2020**, *36*, 101538. [[CrossRef](#)]
21. Gong, H.; Nadimpalli, V.K.; Rafi, K.; Starr, T.; Stucker, B. Micro-CT evaluation of defects in Ti-6Al-4V parts fabricated by metal additive manufacturing. *Technologies* **2019**, *7*, 44. [[CrossRef](#)]
22. Arvieu, C.; Galy, C.; Le Guen, E.; Lacoste, E. Relative density of SLM-produced aluminum alloy parts: Interpretation of results. *J. Manuf. Mater. Process.* **2020**, *4*, 83. [[CrossRef](#)]
23. Facfox. Selective Laser Melting—The Ultimate Guide. 2022. Available online: <https://facfox.com/docs/kb/selective-laser-melting-the-ultimate-guide> (accessed on 2 September 2022).
24. Rickenbacher, L.; Spierings, A.; Wegener, K. An integrated cost-model for selective laser melting (SLM). *Rapid Prototyp. J.* **2013**, *19*, 208–214. [[CrossRef](#)]
25. Maskery, I.; Aboulkhair, N.T.; Corfield, M.R.; Tuck, C.; Clare, A.T.; Leach, R.K.; Wildman, R.D.; Ashcroft, I.A.; Hague, R.J. Quantification and characterisation of porosity in selectively laser melted Al-Si10-Mg using X-ray computed tomography. *Mater. Charact.* **2016**, *111*, 193–204. [[CrossRef](#)]
26. Feng, S.; Chen, Z.; Bircher, B.; Ji, Z.; Nyborg, L.; Bigot, S. Predicting laser powder bed fusion defects through in-process monitoring data and machine learning. *Mater. Des.* **2022**, *222*, 111115. [[CrossRef](#)]
27. MathWorks-1. Overlay Image on Top of Image. Available online: <https://www.mathworks.com/matlabcentral/answers/414351-overlay-image-on-top-of-image> (accessed on 4 October 2022).
28. MathWorks-2. Structural Similarity (SSIM) Index for Measuring Image Quality. Available online: <https://uk.mathworks.com/help/images/ref/ssim.html> (accessed on 27 July 2022).
29. MathWorks-3. Adapthresh. Available online: <https://uk.mathworks.com/help/images/ref/adapthresh.html> (accessed on 2 September 2022).
30. Hui, J. Convolutional Neural Networks (CNN) Tutorial. 2017. Available online: <https://jhui.github.io/2017/03/16/CNN-Convolutional-neural-network> (accessed on 15 November 2021).
31. MathWorks-3. Convolutional Neural Network. Available online: <https://uk.mathworks.com/solutions/deep-learning/convolutional-neural-network.html> (accessed on 7 October 2019).
32. Yamashita, R.; Nishio, M.; Do, R.K.G.; Togashi, K. Convolutional neural networks: An overview and application in radiology. *Insights Imaging* **2018**, *9*, 611–629. [[CrossRef](#)] [[PubMed](#)]
33. McDermott, J. Convolutional Neural Networks—Image Classification w. Keras. 2021. Available online: <https://www.learndatasci.com/tutorials/convolutional-neural-networks-image-classification> (accessed on 15 November 2021).
34. Brownlee, J. Understand the Impact of Learning Rate on Neural Network Performance. 2020. Available online: <https://machinelearningmastery.com/understand-the-dynamics-of-learning-rate-on-deep-learning-neural-networks/> (accessed on 29 November 2021).
35. Ouf, H. Maxpooling vs. Minpooling vs. Average Pooling. 2017. Available online: <https://hany-ouf.blogspot.com/2020/08/maxpooling-vs-minpooling-vs-average.html> (accessed on 15 November 2021).
36. MathWorks-4. Training Options SGDM. Available online: <https://uk.mathworks.com/help/deeplearning/ref/nnet.cnn.trainingoptionssgdm.html> (accessed on 15 November 2021).
37. MathWorks-5. Deep Learning Using Bayesian Optimization. Available online: <https://www.mathworks.com/help/deeplearning/ug/deep-learning-using-bayesian-optimization.html> (accessed on 4 April 2020).
38. Al-Musawi, A. The Development of New Artificial Intelligence Based Hybrid Techniques Combining Bees Algorithm, Data Mining and Genetic Algorithm for Detection, Classification and Prediction of Faults in Induction Motors. Ph.D. Thesis, Cardiff University, Cardiff, UK, 2019.
39. MathWorks-6. Bees Algorithm (BeA) in MATLAB. Available online: <https://uk.mathworks.com/matlabcentral/fileexchange/52967-bees-algorithm-bea-in-matlab> (accessed on 9 April 2020).